*J. Fluid Mech.* (2013), *vol.* 727, *pp.* 132–160.  
doi:10.1017/jfm.2013.256

# The nonlinear problem of a gliding body with gravity

**Y. A. Semenov**[1,2] **and G. X. Wu**[1,†]

[1]Department of Mechanical Engineering, University College London, London WC1E 6BT, UK
[2]Institute of Hydromechanics of the NAS of Ukraine, Kiev 03057, Ukraine

(Received 10 October 2012; revised 14 May 2013; accepted 20 May 2013;
first published online 14 June 2013)

Analysis based on the velocity potential free flow theory with the fully nonlinear boundary condition is made for the steady flow generated by a body gliding along a free surface. Employing the integral hodograph method, we derive analytical expressions for the complex velocity and for the derivative of the complex potential with the coordinate of a parameter plane. The boundary value problem is transformed into a system of two integro-differential equations for the velocity modulus on the free surface and for the slope of the wetted body surface in the parameter plane. The same slope and curvature of the free surface and the body surface at the intersection are adopted to determine the separation points of the flow and from the body. Numerical results are provided for a gliding flat plate and a circular cylinder. The pressure distribution along the body and the free surface shape are presented for a wide range of Froude numbers, within the limit for which the solution corresponding to non-breaking waves downstream can be obtained.

**Key words:** surface gravity waves, waves/free-surface flows

## 1. Introduction

Modelling of flows passing a body floating on a free surface is one of the classic problems in fluid mechanics, which started to receive much attention as early as the 19th century. One of the motivations was primarily to increase the speed of ships. This was a huge challenge because the density of water is about 800 times that of air. This remains a big challenge even today. In fact, whereas the speed of aircraft has increased by several magnitudes, the increase of the speed of ships is very much limited, while world trade is still overwhelmingly by sea. Today, rather than single-mindedly pushing up the speed, low-carbon shipping, or green shipping, has become increasingly important. All these require insightful and detailed understanding of ship wave structure, and how to control and minimize wave making by a ship.

The development of high-speed gliding and hydrofoil craft, and wing-in-ground/wave effect craft, as well as the landing on water of sea/air planes, all require research into gliding flows to predict hydrodynamic characteristics at cruising speed or in accelerating and decelerating regimes of hydro/air craft motion. The hydrodynamic force, especially lift, plays a key role in the performance of the craft. Owing to significant change of the wetted surface and the deformation of the free

† Email address for correspondence: g.wu@ucl.ac.uk

surface, nonlinear effects are hugely important and must be accounted for. This is the motivation of the present work.

Another type of flow leading to a similar mathematical problem is bow or stern flow of a ship. In such flows, the gravity effect becomes more important due to lower Froude number, and the shape of the body also plays a key role in the resistance caused by generated surface waves. Extensive efforts have been made in the search for the waveless ship. Typical examples include Chen & Wei (1994) for the three-dimensional (3D) case and Vanden-Broeck (1980, 2010) for the two-dimensional (2D) case based on the nonlinear analysis for flows past corner-shaped semi-infinite bodies with constant draught. In most cases, a practical ship will inevitably generate a wave. The wave usually has many components, among which is the bow wave. Under certain conditions, the bow wave may overturn and break in the form of a splash jet. This is one focus of the present work.

The wave splash can sometimes occur ahead of a ship bow. Dagan & Tulin (1972) proposed a flow model that includes a splash jet rising along the bow, which is cut in the numerical computation. The overall flow topology is similar to Green's (1936) solution for a gliding plate without gravity. Latorre & Ryan (1990) undertook an experiment for an inclined flat plate with the fixed draught of its trailing edge and established the dependence of the angle of the splash jet relative to the inclined plate as a function of the Froude number based on the draught and velocity of the incoming flow. Dias & Vanden-Broeck (1993) modified Dagan & Tulin's (1972) scheme and developed a fully nonlinear model in which the splash jet is formed by a layer of water rising along the bow to its possible maximum value and falling down without interaction with the incoming flow, assuming mathematically that the jet falls onto the second Riemann sheet. We should point out that such a model adopted in the present study is applicable to when the impact of the splash jet does not significantly change the incoming flow, i.e. the interaction between the splash jet and incoming flow can be neglected. This can be justified when the jet is sufficiently thin and its flow rate is sufficiently small, or the jet falls back to the main flow sufficiently far away from the body. This is confirmed by the numerical results obtained in this study.

For the problem of flow passing a floating body, the consideration must include both the bow and stern flow regions because of strong interaction between them. For gliding flows, the speed is usually much higher and the lift (the vertical force) becomes much more significant. As a result, the body may be lifted up. The free surface before the body may rise significantly, which provides a balance between the fluid inertial and the gravity force. It is possible that the whole body is above the undisturbed free surface but it is still in touch with the incoming free surface. In the limiting case of infinite Froude number or zero gravity, the body could tend to infinity above the undisturbed water surface but is still in touch with the liquid. That is, in fact, the so-called Green's paradox (Green 1936).

The problem of a surface-piercing body moving at lower Froude number along the free surface and the problem of a gliding body at large Froude number can be represented by the same mathematical problem. However, owing to the complexity of the mathematical formulation caused by nonlinearity and the unknown free boundary, additional assumptions are usually introduced for each of these problems

and simplification is made accordingly to study the specific flow characteristics of each case. A typical example is to introduce linearization, in which the free surface boundary condition is imposed on its undisturbed position and all the nonlinear terms are ignored. The linearized theory of a gliding flat plate with gravity effect has been addressed by many authors, in particular, Wagner (1932), Sedov (1937), Kochin (1938) and Tuck (1982*a*,*b*).

Fully 2D nonlinear solutions were obtained for a corner-shaped geometry of a semi-infinite body with constant draught by Vanden-Broeck & Tuck (1977), Vanden-Broeck, Schwartz & Tuck (1978) and Vanden-Broeck (1980, 2010). Such solutions are applicable to study flows near the bow or stern regions separately with prescribed position of flow separation from the body. We note that both the bow and stern flows represent the same mathematical problem.

In this paper we attempt to solve the fully nonlinear 2D problem for gliding bodies moving along a free surface. The chosen flow topology is similar to that proposed by Dagan & Tulin (1972), in which the splash jet rises along the bow, separates from the body at some point and falls into the second Riemann sheet mathematically without interacting physically with the incoming flow. The positions of flow separation of the splash jet from the bow as well as separation of the main flow from the back part of the body are unknown *a priori* and should be determined as a part of the solution, together with the draught of the body.

Our solution method, namely the integral hodograph method, is an extension of that proposed by Joukovskii (1890) and further developed by Chaplygin (1910) for solving free streamline flows of an ideal fluid. The core of the method consists of the analytical derivation of two governing functions: the complex velocity and the derivative of the complex potential defined in an auxiliary region, for which it is chosen as the first quadrant of the parameter plane. The integral hodograph method makes it possible to derive the complex velocity function accounting for the variation of the velocity magnitude along the free surface and the variation of the velocity direction along the wetted part of the body in the parameter plane. This method has already been applied to solving various free boundary flows (Semenov & Cummings 2006; Semenov & Iafrati 2006; Faltinsen & Semenov 2008). Here, the problem is formulated based on this method in § 2, where the governing functions are derived.

The boundary value problem in the present study is subsequently transformed into a system of integro-differential equations in terms of the velocity modulus along the free boundaries and the velocity angle along the body surface, both written as a function of parametric variables. These equations are obtained by exploiting the dynamic and kinematic boundary conditions on the free surface and the given shape of the body in the physical plane. They are solved using procedures of numerical integration and successive approximations, as outlined in § 3.

Two body geometries, a flat plate and a circular cylinder, have been considered in this paper as case studies. In the former the focus is on splash jet separation from the bow as the rear separation point is fixed at the trailing edge of the plate. In the latter case the problem involving both bow and stern flow separations is solved, while the locations of both these separation points are part of the solution. Extensive results for free surface shape and the pressure distribution along the wetted part of the body are provided for non-breaking waves.

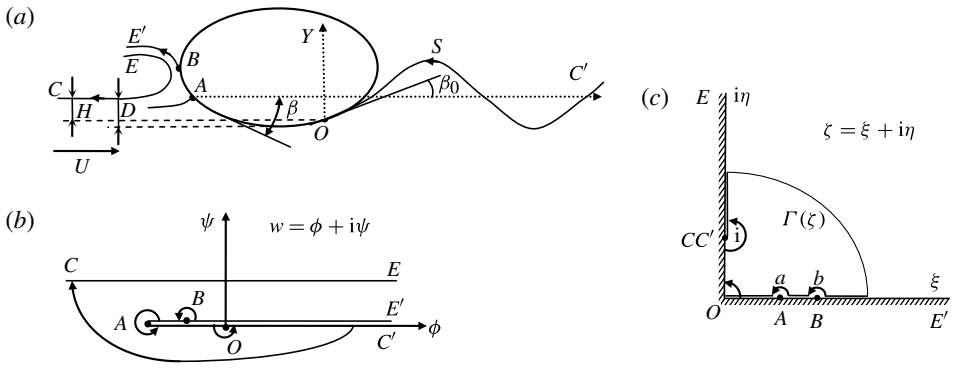


FIGURE 1. Sketch of the problem for a free surface-piercing body in a uniform stream: (*a*) the physical plane; (*b*) the complex potential plane; (*c*) the parameter plane. The strip $BEE'$ in panel (*b*) corresponds to splash jet $BE'E$ in the physical plane, which is cut down or extends onto the second Riemann sheet.

## 2. Theoretical formulation and analysis

Figure 1(*a*) shows the configuration of the problem in which a uniform incoming flow passes a 2D body of arbitrary shape. We focus on the type of problem in which a splash jet forming at the bow (front region) separates from the body. Physically, the jet may overturn and fall back into the main flow due to gravity. Mathematically, the collision of water is not taken into account and the jet is assumed to fall into the second sheet of the Riemann surface (Ahlfors 1966). At the stern (rear region) the main flow separates from the body and forms the wavy free surface downstream. A radiation condition in numerical computations in the form of absorbing the wave is applied at a large distance far behind the body to avoid the influence of wave reflection from the truncated boundary. As a result the flow downstream behind the wave absorption returns to uniform in the computational model.

The fluid is inviscid and incompressible, and the flow is steady and irrotational. The incoming flow is uniform, with a constant velocity $U$, and the free surface there is flat and parallel to the $x$-axis of the Cartesian coordinate system $x$–$y$. The line $y = 0$ corresponds to the undisturbed free surface and the $y$-axis points vertically upwards, and passes through the rear flow separation point $O$ as shown in figure 1(*a*).

The angle $\beta$ in figure 1(*a*) indicates the local tangential direction of the body surface and the upper side of the splash jet $BE'$. The shape of the wetted body surface is given by angle $\beta$ as a function of the spatial coordinate $S$ along the body, between separation points $O$ and $B$. At the stagnation point $A$, the incoming streamline splits into two, which go along the upper and lower sides of the body, respectively. The first streamline leads to a splash jet, and the lower streamline along the body surface detaches at point $O$ and forms the wavy free surface downstream. The Brillouin–Villat criterion is applied to determine the location of the separation points $O$ and $B$. This condition requires the curvatures of the free surface and the body at the point of separation to be the same, in addition to their slopes (Brillouin 1911; Villat 1914).

The Bernoulli equation can be written for a reference point at upstream infinity,

$$\rho\frac{V^2}{2} + \rho g y + p = \rho\frac{U^2}{2} + p_a, \tag{2.1}$$

where $\rho$ is the liquid density, $V$ is the magnitude of the velocity and $p_a$ is the atmospheric pressure. The Froude number can be defined as

$$Fn = \frac{U}{\sqrt{gL}}, \tag{2.2}$$

where $L$ is a characteristic length of the body. In the case of a circular cylinder, we may choose $L = R$, or its radius, while for the case of a flat plate we shall choose another length to be discussed later.

Using non-dimensionalization, (2.1) takes the form

$$v^2 = 1 - c_p - \frac{2y}{Fn^2}, \tag{2.3}$$

where $c_p = 2(p - p_a)/\rho U^2$ is the pressure coefficient, and $h = H/L$, $v = V/U$, $x = X/L$, $y = Y/L$ are the dimensionless immersion, velocity magnitude, and horizontal and vertical coordinates, respectively. Equation (2.3) gives the velocity magnitude along the free surface, where $c_p = 0$, if the coordinate $y$ is known.

### 2.1. *Expressions for complex velocity and derivative of complex potential*

In order to derive expressions for the complex velocity and the complex potential (or its derivative), we choose the first quadrant of the parameter plane $\zeta = \xi + \mathrm{i}\eta$ shown in figure 1(*c*), to correspond to the fluid domain in the physical plane $z = x + \mathrm{i}y$. If these expressions are known functions of the parameter variable $\zeta$, the velocity field and the function mapping the parameter plane onto the physical plane can be determined as follows (Joukovskii 1890):

$$v_x(\xi, \eta) - \mathrm{i}v_y(\xi, \eta) = \frac{\mathrm{d}w}{\mathrm{d}z}(\zeta), \tag{2.4}$$

where $z_0$ corresponds to point $O$ in the physical plane of figure 1(*a*). A conformal mapping allows us to arbitrarily fix three points $O$, $C$ ($C'$) and $E$ ($E'$) in the parameter plane. Among these, points $C'$ and $C$ corresponding to infinity upstream and downstream in the physical plane, respectively, are the same point $\zeta = \mathrm{i}$ in the parameter plane, and points $E$ ($E'$) for the tip of the splash jet in the physical plane are the two points at infinity in the parameter plane shown in figure 1(*c*). Then $\zeta = a$ and $\zeta = b$ on the real axis of the parameter plane are the images of points $A$ and $B$ in the physical plane, which should be determined from additional conditions. The interval $0 < \eta < 1$ of the imaginary axis corresponds to the free boundary $OC'$ (the region of the downstream flow), and the interval $1 < \eta < \infty$ corresponds to the free surface $CE$. The real axis $0 < \xi < b$ corresponds to the wetted part $OAB$ of the body and $b < \xi < \infty$ corresponds to the upper side of the splash jet. Since the actual range of the complex velocity is unknown *a priori*, an explicit conformal transformation of the first quadrant of the parameter plane onto the complex velocity plane at this stage is a difficult problem.

In the physical plane, the velocity magnitude on the free surface can be expressed from the Bernoulli equation, while the velocity argument on the body surface can be determined by its shape. At this stage, we write the magnitude of the complex velocity on the free boundaries as a function of the parameter variable $\eta$ and its argument on the wetted part of the body and the upper surface of the splash jet as a function of the parameter variable $\xi$. In other words we assume that the function $\mathrm{d}w/\mathrm{d}z$ satisfies the

following boundary conditions:

$$\left|\frac{\mathrm{d}w}{\mathrm{d}z}\right|_{\zeta=\mathrm{i}\eta} = v(\eta), \quad 0<\eta<\infty, \tag{2.5}$$

$$\arg\left(\left.\frac{\mathrm{d}w}{\mathrm{d}z}\right|_{\zeta=\xi}\right) = \gamma(\xi) = \begin{cases} -\pi-\beta, & 0<\xi<a, \\ -\beta, & a<\xi<\infty. \end{cases} \tag{2.6}$$

The argument of the complex velocity undergoes a step change at the point $\zeta = a$ corresponding to the splitting streamline at the stagnation point $A$ in the physical plane. The problem is then to find the function $\mathrm{d}w/\mathrm{d}z$ in the first quadrant of the parameter plane which satisfies the boundary conditions in (2.5) and (2.6). The integral formula derived previously by Semenov (2003) and Semenov & Cummings (2006),

$$\frac{\mathrm{d}w}{\mathrm{d}z} = v_\infty \exp\left[\frac{1}{\pi}\int_0^\infty \frac{\mathrm{d}\gamma}{\mathrm{d}\xi}\ln\left(\frac{\zeta+\xi}{\zeta-\xi}\right)\mathrm{d}\xi - \frac{\mathrm{i}}{\pi}\int_0^\infty \frac{\mathrm{d}\ln v}{\mathrm{d}\eta}\ln\left(\frac{\zeta-\mathrm{i}\eta}{\zeta+\mathrm{i}\eta}\right)\mathrm{d}\eta + \mathrm{i}\gamma_\infty\right], \tag{2.7}$$

where $v_\infty = \lim_{\eta\to\infty} v(\eta)$ and $\gamma_\infty = \lim_{\xi\to\infty}\gamma(\xi)$, provides the solution of the boundary value problem (2.5) and (2.6). Substituting (2.6) into (2.7) and taking into account that $\arg(\zeta-\mathrm{i}\eta) = \arg(\mathrm{i}\eta-\zeta)-\pi$ for the second integral in (2.7), we obtain the expression of the complex velocity defined in the first quadrant of the $\zeta$-plane as

$$\frac{\mathrm{d}w}{\mathrm{d}z} = v_0\left(\frac{\zeta-a}{\zeta+a}\right)\exp\left[-\frac{1}{\pi}\int_0^\infty \frac{\mathrm{d}\beta}{\mathrm{d}\xi}\ln\left(\frac{\xi+\zeta}{\xi-\zeta}\right)\mathrm{d}\xi - \frac{\mathrm{i}}{\pi}\int_0^\infty \frac{\mathrm{d}\ln v}{\mathrm{d}\eta}\ln\left(\frac{\mathrm{i}\eta-\zeta}{\mathrm{i}\eta+\zeta}\right)\mathrm{d}\eta - \mathrm{i}\beta_0\right], \tag{2.8}$$

where $v_0$ and $\beta_0$ are the velocity magnitude and direction at point $O$.

For steady free boundary flows, the stream function $\psi(x, y)$ takes constant values along the body and free boundaries, and therefore the region boundary in the $w$-plane forms a polygonal region shown in figure 1(*b*). According to Chaplygin's singular point method presented in Gurevich (1965), to determine the function $w = w(\zeta)$, it is sufficient to analyse all singular points where the mapping is not conformal. The function $w = w(\zeta)$ has singularities at points $A$ ($\zeta = a$) and $C$ ($\zeta = \mathrm{i}$), which correspond to the corner points of the flow region in the $w$-plane. On going around an infinitesimal semicircle centred at the point $\zeta = a$ of the $\zeta$-plane, $\arg(\zeta-a)$ changes by $\pi$ while the corresponding change of $\arg(w-w_A)$ in the $w$-plane is $2\pi$, as seen from figure 1(*b*), which means that the function $w(\zeta)$ behaves as $(w-w_A)\sim(\zeta-a)^2$. Similarly, on going in the clockwise direction around an infinitesimal semicircle centred at the point $\zeta = \mathrm{i}$, $\arg(\zeta-\mathrm{i})$ increases by $\pi$, while $\arg(w-w_C)$ of the semicircle of large radius connecting points $C'$ and $C$ in the $w$-plane decreases by $\pi$. Therefore, the function $w(\zeta)$ behaves as $(w-w_C)\sim(\zeta-\mathrm{i})^{-1}$. The additional singularity, as a zero of the second order, appears at point $O$ due to the corner of $\pi/2$ in the $\zeta$-plane. On going around an infinitesimal semicircle centred at the point $O$, $\zeta = 0$, $\arg\zeta$ changes by $\pi/2$, while the corresponding change of $\arg(w-w_O)$ in the $w$-plane is $\pi$, as seen from figure 1(*b*,*c*). Therefore, the function $w(\zeta)$ at point $O$ behaves as $(w-w_O)\sim\zeta^2$. In order to satisfy the boundary condition $\mathrm{Im}(w) = \text{const.}$ on the whole flow boundary, it is necessary to put singularities of the same order in the symmetric points $\zeta = -a$ and $\zeta = -\mathrm{i}$. By differentiating the function $w(\zeta)$, we obtain that the derivative $\mathrm{d}w/\mathrm{d}\zeta$ has the following singularities: $\zeta$, $(\zeta-a)$, $(\zeta+a)$, $(\zeta-\mathrm{i})^{-2}$ and $(\zeta+\mathrm{i})^{-2}$. There are no other singularities in the function $\mathrm{d}w/\mathrm{d}\zeta$, and therefore we can use Liouville's

theorem to determine the expression $\mathrm{d}w/\zeta$ as

$$\frac{\mathrm{d}w}{\mathrm{d}\zeta} = K\frac{\zeta(\zeta^2 - a^2)}{(\zeta^2+1)^2}, \tag{2.9}$$

where $K$ is a real scale factor. Dividing (2.9) by (2.8), we obtain the derivative of the mapping function as

$$\frac{\mathrm{d}z}{\mathrm{d}\zeta} = \frac{K}{v_0}\frac{\zeta(\zeta+a)^2}{(\zeta^2+1)^2}\exp\left[\frac{1}{\pi}\int_0^\infty \frac{\mathrm{d}\beta}{\mathrm{d}\xi}\ln\left(\frac{\xi+\zeta}{\xi-\zeta}\right)\mathrm{d}\xi + \frac{\mathrm{i}}{\pi}\int_0^\infty \frac{\mathrm{d}\ln v}{\mathrm{d}\eta}\ln\left(\frac{\mathrm{i}\eta-\zeta}{\mathrm{i}\eta+\zeta}\right)\mathrm{d}\eta + \mathrm{i}\beta_0\right], \tag{2.10}$$

whose integration along the imaginary axis in the parameter region on intervals $0<\eta<1$ and $1<\eta<\infty$ provides the free boundaries $OC'$ and $CE$ in the $z$-plane. It is implied that the free surface obtained by integrating (2.10) satisfies the kinematic boundary condition, since $\mathrm{Im}(w)=0$ on both the solid and free boundaries. The parameters $a$, $b$ and $K$ and the functions $v(\eta)$ and $\beta(\xi)$ have to be determined from the boundary conditions and from physical considerations.

At upstream infinity in the physical plane, and $\zeta=\mathrm{i}$ in the parameter plane, the inflow velocity approaches the value $v_c = v(\eta)|_{\eta=1} = 1$ along the $x$-axis. When the wave absorbing condition is imposed, the flow at downstream infinity will also be uniform. By taking the argument of the complex velocity in (2.8) when $\zeta=\mathrm{i}$, we obtain the following equation:

$$\frac{1}{\pi}\int_0^\infty \frac{\mathrm{d}\ln v}{\mathrm{d}\eta}\ln\left|\frac{\eta-1}{\eta+1}\right|\mathrm{d}\eta + \frac{2}{\pi}\int_0^\infty \frac{\mathrm{d}\beta}{\mathrm{d}\xi}\tan^{-1}\left(\frac{1}{\xi}\right)\mathrm{d}\xi + 2\tan^{-1}\left(\frac{2}{a}\right) + \beta_0 - \pi = 0. \tag{2.11}$$

We denote the length along the body surface in the physical plane between stagnation point $A$ and point $O$ as $S_A$. We have

$$s_A = \int_0^a \frac{\mathrm{d}s}{\mathrm{d}\xi}\mathrm{d}\xi, \tag{2.12}$$

where $s_A = S_A/L$ and

$$\frac{\mathrm{d}s}{\mathrm{d}\xi} = \left|\frac{\mathrm{d}z}{\mathrm{d}\zeta}\right|_{\zeta=\xi} \tag{2.13}$$

can be obtained from (2.10). By integrating (2.10) in the parameter plane along an arbitrary line $\Gamma(\zeta)$ linking points $O$ and $C$, the imaginary part of the integral should give $h$, where $-h$ is the vertical ordinate of the point $O$ as shown in figure 1(*a*). Here we use

$$\mathrm{Im}\left\{\int_0^{\xi^*}\left.\frac{\mathrm{d}z}{\mathrm{d}\zeta}\right|_{\zeta=\xi}\mathrm{d}\zeta + \int_{(\xi^*,0)}^{(0,\mathrm{i}\eta^*)}\frac{\mathrm{d}z}{\mathrm{d}\zeta}\mathrm{d}\zeta + \int_{\eta^*}^1\left.\frac{\mathrm{d}z}{\mathrm{d}\zeta}\right|_{\zeta=\mathrm{i}\eta}\mathrm{d}\eta\right\} = h, \tag{2.14}$$

where the line $\Gamma(\zeta)$ consists of intervals, $0<\xi<\xi^*$, $\eta=0$, and $1<\eta<\xi^*$, $\xi=0$, and the arc of a circle of large radius $\xi^*$ linking the real and imaginary axes of the

parameter region (see figure 1*c*). If the length $s_A$ is given, then (2.11), (2.12) and (2.14) allow us to determine the unknown parameters $a$, $K$ and the vertical coordinate of the point $O$, $-h$.

### 2.2. *System of integro-differential equations*

#### 2.2.1. *Body surface boundary condition: integro-differential equation for function $\beta(\xi)$ in interval $0 < \xi < b$*

By integrating the modulus of (2.10) along the real axis of the parameter region, we can determine the spatial coordinate along the body as a function of the parameter variable

$$s(\xi) = \int_0^{\xi} \frac{\mathrm{d}s}{\mathrm{d}\xi'}\,\mathrm{d}\xi'. \tag{2.15}$$

Since the function $\beta = \beta(s)$ is known on the wetted body surface $OB$ corresponding to the interval $0 < \xi < b$, the function $\beta = \beta(\xi)$ is determined from the following equation:

$$\frac{\mathrm{d}\beta}{\mathrm{d}\xi} = \frac{\mathrm{d}\beta}{\mathrm{d}s}\frac{\mathrm{d}s}{\mathrm{d}\xi}. \tag{2.16}$$

By using $\mathrm{d}s/\mathrm{d}\xi$ from (2.13), this equation takes the form

$$\frac{\mathrm{d}\beta}{\mathrm{d}\xi} = \frac{K}{v_0}\kappa[s(\xi)]\frac{\xi(\xi+a)^2}{(\xi^2+1)^2} \times \exp\left[\frac{1}{\pi}\int_0^{\infty}\frac{\mathrm{d}\beta}{\mathrm{d}\xi'}\ln\left|\frac{\xi+\xi'}{\xi-\xi'}\right|\mathrm{d}\xi' + \frac{2}{\pi}\int_0^{\infty}\frac{\mathrm{d}\ln v}{\mathrm{d}\eta}\tan^{-1}\left(\frac{\eta}{\xi}\right)\mathrm{d}\eta\right], \tag{2.17}$$

where $\kappa(s) = \mathrm{d}\beta/\mathrm{d}s$ is the body curvature.

### 2.3. *Free surface boundary condition: integro-differential equation for function $\mathrm{d}\ln v/\mathrm{d}\eta$ in interval $0 < \eta < \infty$*

Differentiating the Bernoulli equation in (2.3) along the free surface with respect to the spatial coordinate, we obtain

$$v\frac{\mathrm{d}v}{\mathrm{d}s} + \frac{1}{Fn^2}\sin\delta = 0, \tag{2.18}$$

where $\sin\delta = \mathrm{d}y/\mathrm{d}s$ is the slope to the free surface coinciding with the velocity direction relative to the $x$-axis. The angle $\delta$ can be determined from the expression for the complex velocity, or $\delta = -\arg(\mathrm{d}w/\mathrm{d}z)|_{\zeta=\mathrm{i}\eta}$. Taking the argument in (2.3) when $\zeta = \mathrm{i}\eta$, we obtain

$$\delta(\eta) = \frac{2}{\pi}\int_0^{\infty}\frac{\mathrm{d}\beta}{\mathrm{d}\xi}\tan^{-1}\frac{\eta}{\xi}\,\mathrm{d}\xi + \frac{1}{\pi}\int_0^{\infty}\frac{\mathrm{d}\ln v}{\mathrm{d}\eta'}\ln\left|\frac{\eta'-\eta}{\eta'+\eta}\right|\mathrm{d}\eta' + 2\tan^{-1}\frac{\eta}{a} + \pi - \beta_0. \tag{2.19}$$

Using the relations

$$\frac{\mathrm{d}v}{\mathrm{d}s} = v\frac{\mathrm{d}\ln v}{\mathrm{d}\eta}\Big/\frac{\mathrm{d}s}{\mathrm{d}\eta} \tag{2.20}$$

and

$$\frac{\mathrm{d}s}{\mathrm{d}\eta} = \left|\frac{\mathrm{d}z}{\mathrm{d}\eta}\right|_{\zeta=\mathrm{i}\eta} = \frac{K}{v(\eta)}\frac{\eta(\eta^2+a^2)}{(1-\eta^2)^2}, \tag{2.21}$$

we can rewrite the boundary condition in (2.18) with the following integro-differential equation in terms of the function $\mathrm{d}(\ln v)/\mathrm{d}\eta$ over the interval $0<\eta<\infty$:

$$Fn^2v^3\frac{\mathrm{d}\ln v}{\mathrm{d}\eta} + K\frac{\eta(\eta^2+a^2)}{(1-\eta^2)^2}\sin\left[\frac{1}{\pi}\int_0^\infty \frac{\mathrm{d}\ln v}{\mathrm{d}\eta'}\ln\left|\frac{\eta'-\eta}{\eta'+\eta}\right|\mathrm{d}\eta' + P(\eta)\right] = 0, \tag{2.22}$$

where

$$P(\eta) = \frac{2}{\pi}\int_0^\infty \frac{\mathrm{d}\beta}{\mathrm{d}\xi}\tan^{-1}\frac{\eta}{\xi}\,\mathrm{d}\xi + 2\tan^{-1}\frac{\eta}{a} + \pi - \beta_0, \tag{2.23}$$

$$v(\eta) = v_0\exp\left(\int_0^\eta \frac{\mathrm{d}\ln v}{\mathrm{d}\eta'}\mathrm{d}\eta'\right), \quad v_0 = \sqrt{1+\frac{2(1+h)}{Fn^2}}. \tag{2.24}$$

### 2.4. *Free surface boundary condition on upper surface of jet: integral equation for function $\beta(\xi)$ in interval $b<\xi<\infty$*

Let the function $y(\xi)$ be the vertical coordinate of the upper surface of the jet $BE'$ obtained by integrating (2.10). Using the Bernoulli equation on the free surface with $c_p = 0$ and through some algebraic manipulation, we obtain the following integral equation for the function $\beta(\xi)$, within $b<\xi<\infty$:

$$\frac{1}{\pi}\int_b^\infty \frac{\mathrm{d}\beta}{\mathrm{d}\xi'}\ln\left|\frac{\xi'+\xi}{\xi'-\xi}\right|\mathrm{d}\xi' = \ln\left(\frac{v_0}{\widetilde{v}(\xi)}\frac{\xi-a}{\xi+a}\right) - \frac{1}{\pi}\int_0^b \frac{\mathrm{d}\beta}{\mathrm{d}\xi'}\ln\left|\frac{\xi'+\xi}{\xi'-\xi}\right|\mathrm{d}\xi' + \frac{2}{\pi}\int_b^\infty \frac{\mathrm{d}\ln v}{\mathrm{d}\eta}\tan^{-1}\left(\frac{\xi}{\eta}\right)\mathrm{d}\eta, \tag{2.25}$$

where, from (2.3),

$$\widetilde{v}(\xi) = \sqrt{1-\frac{2y(\xi)}{Fn^2}}, \tag{2.26}$$

with $y(\xi)$ being obtained from (2.10), while the function $\mathrm{d}(\ln v)/\mathrm{d}\eta$ along the imaginary axis of the parameter plane is obtained from (2.22).

In summary, the function of the velocity magnitude $v(\eta)$ is determined by (2.22) on the whole imaginary axis of the parameter plane, while the function $\beta(\xi)$ is determined from the integro-differential equation in (2.17) on the interval $0<\xi<b$ and from the integral equation (2.25) on the rest of the real axis $b<\xi<\infty$. The parameter $b$ is determined from the Brillouin–Villat condition to be discussed later in detail.

### 2.5. *Asymptotic equations for the tip of the splash jet*

The tip region of the splash jet is mapped to $|\zeta|\to\infty$ in the parameter plane, as seen from figure 1(*c*), which presents some computational difficulties. To overcome this, we make a variable change. We notice that the asymptotic expression for the complex potential and its derivative can be obtained from (2.9) for $|\zeta|\to\infty$,

$$\frac{\mathrm{d}w}{\mathrm{d}\zeta} = \frac{K}{\zeta}, \quad w = w^* + K\ln\zeta, \quad |\zeta|\geqslant\xi^*, \tag{2.27}$$

where $\xi^* \gg a$ is some large value and $w^* = K\int_0^{\xi^*}(\xi(\xi^2 - a^2)/(\xi^2 - 1)^2)\,\mathrm{d}\xi$. From (2.27) it is possible to express the parameter variable $\zeta$ as a function of the complex potential,

$$\zeta(w) = \xi^* \exp\left(\frac{w - w^*}{K}\right). \tag{2.28}$$

The imaginary part of the complex potential $w = \phi + \mathrm{i}\psi$ may change in the range $0 \leqslant \psi \leqslant q$ (see figure 1*b*), from the lower surface to the upper surface of the splash jet, where $q = \pi K/2$ is the flow rate of the splash jet, which is obtained using the residue theorem when integrating (2.27) in the parameter plane along an arc of a circle of infinite radius from $E'$ to $E$.

By substituting (2.28) into (2.8) we obtain the complex velocity as a function of the complex potential $w$ in the following form:

$$\frac{\mathrm{d}w}{\mathrm{d}z}(w) = v_0 \exp\left[-\frac{1}{\pi}\int_0^{\xi^*}\frac{\mathrm{d}\beta}{\mathrm{d}\xi}\ln\left(\frac{\xi + \zeta(w)}{\xi - \zeta(w)}\right)\mathrm{d}\xi - \frac{1}{\pi}\int_{\phi^*}^{\infty}\frac{\mathrm{d}\beta}{\mathrm{d}\phi}\ln\left(\frac{\xi(\phi) + \zeta(w)}{\xi(\phi) - \zeta(w)}\right)\mathrm{d}\phi \right.$$
$$\left. - \frac{\mathrm{i}}{\pi}\int_0^{\xi^*}\frac{\mathrm{d}\ln v}{\mathrm{d}\eta}\ln\left(\frac{\mathrm{i}\eta - \zeta(w)}{\mathrm{i}\eta + \zeta(w)}\right)\mathrm{d}\eta - \frac{\mathrm{i}}{\pi}\int_{\phi^*}^{\infty}\frac{\mathrm{d}\ln v}{\mathrm{d}\phi}\ln\left(\frac{\mathrm{i}\eta(\phi) - \zeta(w)}{\mathrm{i}\eta(\phi) + \zeta(w)}\right)\mathrm{d}\phi\right], \tag{2.29}$$

where

$$\left.\begin{aligned}\xi(\phi) &= \xi^* \exp\left(\frac{\phi - \phi^*}{K}\right)\cos\left(\frac{\psi}{K}\right),\\ \eta(\phi) &= \xi^* \exp\left(\frac{\phi - \phi^*}{K}\right)\sin\left(\frac{\psi}{K}\right),\\ \phi^* &= \mathrm{Re}(w^*)\end{aligned}\right\} \tag{2.30}$$

The derivative of the mapping function, $\mathrm{d}z/\mathrm{d}w$, is just the inverse function of the complex velocity in (2.29). By integrating the function $\mathrm{d}z/\mathrm{d}w$ in the plane of the complex potential along the interval $\phi^* < \mathrm{Re}(w) < \infty$, we can evaluate the upper side contour of the splash jet, $y^{up}(\phi)$, where the imaginary part of the complex potential is $\mathrm{Im}(w) = q$, and the lower side, $y^{lw}(\phi)$, where $\mathrm{Im}(w) = 0$. Then, from the Bernoulli equation (2.3), the velocity magnitude on the upper and lower sides of the splash jet near its tip can be written as

$$v^{\{up,lw\}}(\phi) = \sqrt{1 - \frac{2y^{\{up,lw\}}(\phi)}{Fn^2}}, \tag{2.31}$$

where

$$y^{\{up,lw\}}(\phi) = y^{*\{up,lw\}} + \mathrm{Im}\left[\int_{\phi^*}^{\phi}\left.\frac{\mathrm{d}z}{\mathrm{d}w}\right|_{w=\{\phi',w=\phi'+\mathrm{i}q\}}\mathrm{d}\phi'\right], \quad \frac{\mathrm{d}z}{\mathrm{d}w} = \frac{1}{\mathrm{d}w/\mathrm{d}z}, \tag{2.32}$$

and $\mathrm{d}w/\mathrm{d}z$ is obtained from (2.29). By eliminating from (2.25) the parameter variable $\zeta$ using (2.28) and (2.30), we obtain the integral equation for the function $\beta(\phi)$ over the interval $\phi^* < \mathrm{Re}(w) < \infty$, $\mathrm{Im}(w) = q$, corresponding to the upper side of the

splash jet,

$$\frac{1}{\pi}\int_{\phi*}^{\infty}\frac{\mathrm{d}\beta}{\mathrm{d}\phi}\ln\left|\frac{\xi(\phi')+\xi(\phi)}{\xi(\phi')-\xi(\phi)}\right|\mathrm{d}\phi' = \ln\left(\frac{v_0}{v^{up}(\phi)}\right)-\frac{1}{\pi}\int_0^{\xi^*}\frac{\mathrm{d}\beta}{\mathrm{d}\xi'}\ln\left|\frac{\xi'+\xi}{\xi'-\xi}\right|\mathrm{d}\xi' + \frac{2}{\pi}\int_0^{\xi^*}\frac{\mathrm{d}\ln v}{\mathrm{d}\eta}\tan^{-1}\left(\frac{\xi(\phi)}{\eta}\right)\mathrm{d}\eta+\frac{2}{\pi}\int_{\phi*}^{\infty}\frac{\mathrm{d}\ln v^{lw}}{\mathrm{d}\phi'}\tan^{-1}\left(\frac{\xi(\phi)}{\eta(\phi')}\right)\mathrm{d}\phi'. \quad (2.33)$$

The lower side of the splash jet is determined by (2.31) since the velocity magnitude $v(\phi)=v^{lw}(\phi)$ explicitly appears in (2.29) and is evaluated through (2.31) and (2.32).

### 2.6. *Flow detachment*

For bodies with a sharp trailing edge, it is common to assume that the flow separates at the trailing edge, and thus the location of the separation point is known. Therefore, the system of equations derived in the previous sections is closed if all the separation points are known and can be solved numerically. For smoothly shaped bodies, the position of free surface detachment is unknown and should be determined from an additional condition. In the present model, line $AOC'$ (or line $E'BA$) is a single streamline. Here we assume that the line, its first (slope) and second (curvature) derivatives are continuous. This means that (i) $z(w)$, (ii) $\mathrm{d}z/\mathrm{d}w$ and (iii) $\mathrm{d}^2z/\mathrm{d}w^2$ are continuous, along the streamline. Then (ii) and (iii) are equivalent to the velocity and the derivative of the velocity along the streamline being continuous. As a result, we can apply differentiation, $\mathrm{d}c_p/\mathrm{d}s$, along the whole line $AOC'$. Thus, when we approach the separation point from the free surface, we have $\mathrm{d}c_p/\mathrm{d}s=0$ as $c_p=0$ on $OC'$. Equation (2.18) then gives

$$\frac{\mathrm{d}\ln v}{\mathrm{d}s}=-\frac{\sin\delta}{v_0^2Fn^2} \quad (2.34)$$

at point $O$. From (2.10) and (2.13) it can be seen that $\lim_{\xi\to0}(\mathrm{d}s/\mathrm{d}\xi)=0$. Thus we obtain

$$\lim_{\xi\to0}\frac{\mathrm{d}\ln v}{\mathrm{d}\xi}=\lim_{s\to0}\frac{\mathrm{d}\ln v}{\mathrm{d}s}\lim_{\xi\to0}\frac{\mathrm{d}s}{\mathrm{d}\xi}=0. \quad (2.35)$$

Differentiating the function $v(\xi)=|\mathrm{d}w/\mathrm{d}z|_{\zeta=\xi}$ obtained from (2.8) for $\zeta=\xi$, and substituting the result into the left-hand side of (2.35) and taking the limit, we obtain

$$\int_0^{\infty}\frac{\mathrm{d}\beta}{\mathrm{d}\xi}\frac{\mathrm{d}\xi}{\xi}-\int_0^{\infty}\frac{\mathrm{d}\ln v}{\mathrm{d}\eta}\frac{\mathrm{d}\eta}{\eta}+\frac{\pi}{a}=0. \quad (2.36)$$

This is a nonlinear equation, which will be imposed during the solution.

In order to determine flow separation at point $B$, we may make use of

$$\left.\frac{\mathrm{d}c_p}{\mathrm{d}s}\right|_{s=s(b)}=0, \quad (2.37)$$

at $s_b=S_b/L=s(b)$, where $S_b$ is the length of the wetted part of the body. However, further derivation based on (2.34) to provide a condition similar to (2.34) is less straightforward, because the governing equation over $BE'$ is given through $\beta(s)$ in (2.25), not through $\mathrm{d}\ln v/\mathrm{d}s$ as in (2.22) for $OC'$. In the computation after all the

above equations are discretized, (2.37) is imposed numerically. In other words, the derivative is calculated through the difference method. If it is not sufficiently small, it will be updated until the value is small enough. The detailed iteration procedure will be discussed in detail below.

## 3. Results and discussion

### 3.1. *Numerical approach*

In the discrete form, the solution is sought on a given set of points $\xi_i$, $i = 1, \ldots, N$, distributed monotonically along the real axis of the parameter region on the interval $0 < \xi_i < \xi^*$ and a given set of points $\eta_j$, $j = 1, \ldots, M$, distributed along the imaginary axis on the interval $0 < \eta_j < \xi^*$. The value $\xi^*$ is chosen in the range $\xi^* = 10^4$–$10^6$, $N$ in the range of $N = 100$–$300$, and $M$ in the range of $M = 100$–$500$ based on the requirement for the convergence and accuracy of the solution. The points $\xi_i$ and $\eta_j$ are distributed in such a way as to provide a higher density of the points $s_i = s(\xi_i)$ and $s_j = s(\eta_j)$ on the body surface near the separation points, on the free boundary near the separation point $O$ and on the crests of the wave using the refining procedure of the node distribution. The integrals in the system of equations are evaluated analytically over each segment $(\xi_{i-1}, \xi_i)$ or $(\eta_{j-a}, \eta_j)$, on the basis that the functions $\beta(\xi)$ and $\ln v(\eta)$ within the interval can be accurately approximated by linear interpolation. The numerical approach is similar to that presented in Yoon & Semenov (2011).

A numerical radiation condition is needed in the computation. The integral equation in (2.22) is solved over the interval $(0, \eta_R)$, where $1 - \eta_R$ is chosen to be small enough to cover a sufficiently large length $x_R = \mathrm{Re}[z(\eta_R)]$ of the free surface and to ensure that $x_R \gg L$. It is found from computational experience that for the many cases considered in this paper two wavelengths are usually enough to exclude the significant effect of the truncated boundary on the results presented.

From figure 1(*c*) it is seen that infinite upstream and infinite downstream correspond to the same point $\zeta = \mathrm{i}$ or $\eta = 1$ in the parameter plane. In order to calculate the integral in (2.8), we need to provide a constant value of the velocity magnitude in the vicinity of the point $\eta = 1$. This means $v = 1$ at infinity on both the left- and the right-hand sides in the numerical model after a wave absorbing scheme is imposed far downstream. To do that, we introduce an interval $(\eta_R, \eta_T)$, where $\eta_R < \eta_T < 1$, corresponding to a transition interval $(x_R, x_R + \lambda)$ in the physical plane. Then the velocity magnitude along the transition interval is given artificially as

$$v(x) = 1 + A_v \sin[2\pi(x - x_R)/\lambda]\mathrm{e}^{-2(x-x_R)/\lambda}, \tag{3.1}$$

where $x_R < x < x_R + \lambda$, $\lambda = 2\pi Fn^2$, is the length of the linear wave. The velocity magnitude is given by $v(x) \equiv 1$ on the interval $x_R + \lambda < x < \infty$, which corresponds to $(\eta_T, 1)$ in the parameter plane. This is a kind of wave absorbing condition, similar to those commonly used in wave radiation and diffraction problems (e.g. Wang & Wu 2006).

From (2.8), we can find the slope of the free surface,

$$\delta(\eta) = -\arg\left(\frac{\mathrm{d}w}{\mathrm{d}z}\right)_{\zeta=\mathrm{i}\eta} = \delta_1(\eta) + \frac{1}{\pi}\int_{\eta_R}^{\eta_T} \frac{\mathrm{d}\ln v}{\mathrm{d}\eta'} \ln\left|\frac{\eta' - \eta}{\eta' + \eta}\right| \mathrm{d}\eta', \tag{3.2}$$

where

$$\delta_1(\eta) = \pi - 2\tan\frac{\eta}{a} - \frac{2}{\pi}\int_0^{\infty} \frac{\mathrm{d}\beta}{\mathrm{d}\xi} \tan^{-1}\frac{\eta}{\xi}\,\mathrm{d}\xi - \frac{1}{\pi}\int_{0,\eta_T}^{\eta_R,\infty} \frac{\mathrm{d}\ln v}{\mathrm{d}\eta'} \ln\left|\frac{\eta' - \eta}{\eta' + \eta}\right| \mathrm{d}\eta'. \tag{3.3}$$

From (3.2) it is seen that the function of the velocity magnitude in the truncation region given by (3.1) affects the velocity direction and the shape of the whole free surface $y(\eta)$. Thus, parameter $A_v$ in (3.1) should be chosen in such a way that both the kinematic and dynamic free surface boundary conditions are satisfied as accurately as possible. One way to measure that is the mean square difference in the wave elevations obtained from these two conditions,

$$\varepsilon^*(A_v) = \min \sum_{1}^{M_1} (y_j - \widetilde{y}_j)^2, \tag{3.4}$$

where $y_j$ is obtained by integrating (2.10) and $\widetilde{y}_j$ is obtained from the Bernoulli equation (2.10) at $c_p = 0$, and $M_1$ is the number of nodes in the range $0 < x(\eta_j) < x_R$. The integral equations (2.17), (2.22) and (2.25) are solved for each given $s_A$ using the method of successive approximations. The iteration procedure is constructed as follows.

(i) Functions $v(\eta)$ and $\beta(\xi)$ are initialized as $v(\eta) \equiv 1$ and $\beta(\xi) \equiv \beta_0$, together with parameter $A_v = 0$ and $b = b_0 = \xi^*$.

(ii) Equation (2.17) for $\beta(\xi)$ on the body surface, or $0 \leqslant \xi \leqslant b_n$, is solved by iteration for a given function $v(\eta)$. For each iteration, (2.11) is used to update $a$ and (2.12) together with (2.10) and (2.13) to update $K$ at given $s_A$. This is repeated until the difference in $\beta(\xi)$ from both sides of (2.17) is sufficiently small.

(iii) An external iteration will be applied to (2.22) to update $v(\eta)$ on the free surface including the lower surface of the jet. At each iteration step $n$, $\beta(\xi)$ and $v(\eta)$ required on the right-hand side of (2.25) are now obtained from (2.17) and (2.19), respectively, and $\beta(\xi)$ on the left-hand side, corresponding to the upper surface, can be obtained. At the same iteration step $n$, the pressure coefficient $c_p = c_p(\xi)$ has been evaluated numerically on the body surface, from which $G(b_n) = \mathrm{d}c_p/\mathrm{d}s|_s = s(b_n)$ can be calculated and checked against the condition in (2.37). If $G(b_n) \neq 0$, $b_n$ is replaced by $b_n + 1$ through Newton's method based on the variation of $G(b_n) - G(b_{n-1})$. The calculation moves back to step (ii) above and repeats itself until the results have converged.

(iv) When the iteration in steps (ii) and (iii) has led to convergence, the parameter $A_v$ is updated from (3.4). The calculation returns to step (ii) and continues until $A_v$ has converged.

(v) Equation (2.36) for the separation condition $\beta_0$ at point $O$ is checked. If it is not satisfied accurately, $\beta_0$ will be updated in a similar manner as used for $b$ in step (iii) above. For each new value of $\beta_0$ the calculation will restart from step (ii). This continues until all the results have converged.

The upper limits in all the integrations with respect to $\xi$ and $\eta$ in steps (ii) and (v) are $\xi^*$. This follows from integration in (2.8) based on the assumption that the shape of the splash jet in the region $\xi > \xi^*$ and $\eta > \xi^*$ has a negligible effect on the main flow. When iterations of the main flow are completed, (2.31) and (2.33) can be solved together for $v$ and $\beta$ near the splash jet through another iteration. Using the results, the shape of the splash jet far from the body can be obtained. Finally, (2.14) can be used to obtain $h$, and this concludes the solution.

### 3.2. *Planing flat plate*

The solution procedure presented in § 2 can be used to study flow passing a planing flat plate of a given length $L^*$ as a special case. In practical situations, the length $L^*$

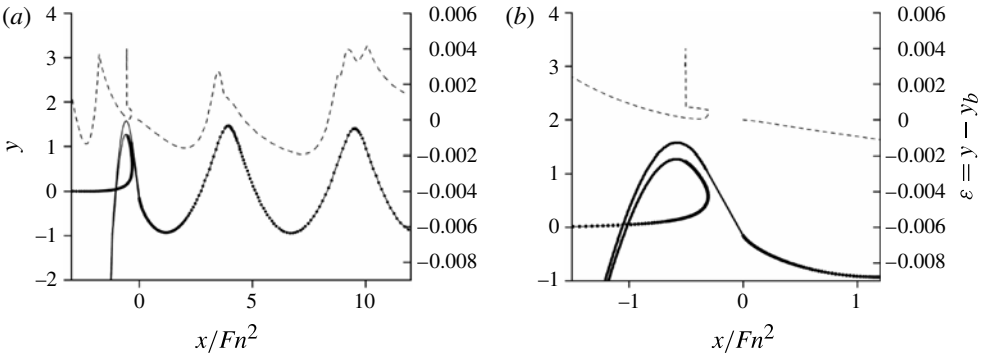


FIGURE 2. (*a*) Free surface (solid line) and difference between wave elevations from kinematic and dynamic boundary conditions $\varepsilon = y - y_b$ (dashed line) for the flat plate with angle of plate $\alpha = 45°$ and Froude number $Fn = 2$. The solid circles indicate the node locations. (*b*) The same near the plate.

should be large enough to ensure that $S_b < L^*$. In this case, the distance between the trailing edge $O$ and the stagnation point $A$, $s_A = S_A/L^*$, is unknown. One way to solve the problem would be to determine $s_A$ from (2.14) for the given immersion $h = H/L^*$ of the trailing edge of the plate. Thus, the solution of the problem depends on three parameters: the Froude number based on the length $L^*$, $Fn_L^*$; the depth of immersion, $h$; and the angle of the plate, $\alpha = -\beta_0$.

Another option, as we do in this paper, is to choose the distance between the trailing edge $O$ and the stagnation point $A$ as a characteristic length $L$, then the parameter $s_A = S_A/L = 1$. As a result, the solution is determined by two parameters, namely the Froude number $Fn$ based on the length $L$, and the angle of plate $\alpha$, as $h$ is a result obtained from solution as discussed at the end of the last section.

The force coefficient perpendicular to the plate is evaluated by integrating the pressure along the wetted part of the plate and non-dimensionalized using the characteristic length $L$. Taking into account (2.3), we obtain

$$C_n = \frac{2F}{\rho U^2 L} = \frac{2}{\rho U^2} \int_0^{s_b} (p - p_a)\, \mathrm{d}s = \int_0^b c_p(\xi) \frac{\mathrm{d}s}{\mathrm{d}\xi}\, \mathrm{d}\xi, \tag{3.5}$$

where $F$ is the normal force.

An example is given in figure 2 for numbers of nodes on the body $N = 200$ and on the free surface $M = 500$, in which the attack angle is defined as $\alpha = -\beta_0$ and the separation point $O$ is fixed at the trailing edge of the plate. The computed free surface shape is presented in the figure together with the difference $\varepsilon = y - y_b$, where $y$ is the free surface obtained by integrating (2.10), and $y_b$ is obtained from the Bernoulli equation in (2.3) with $c_p = 0$. The distribution of nodes used in the computation along the free surface is also shown by solid circles. The figure shows that the error $\varepsilon < 10^{-2}$. All the results presented below are obtained with about the same level of accuracy.

The free surface profiles at different Froude numbers near the plate for different angles of attack is given in figure 3. The wetted part of the plate is shown by the thick solid line. The splash jet separates from the plate and falls under the gravity force. The open circles show the location of the stagnation point. It should be noted that, based on the definition of $L$, the distance from the stagnation point to the trailing edge of

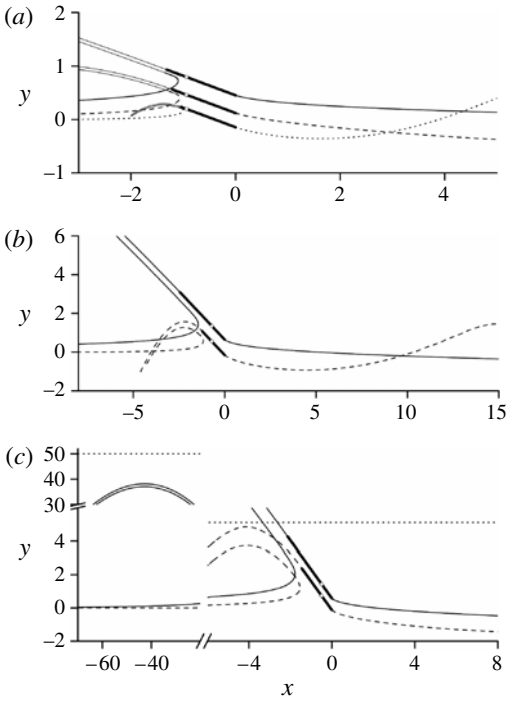


FIGURE 3. The free surface profile near the flat plate, at: (*a*) $\alpha = 20°$, $Fn = 10$ (solid line), $Fn = 3$ (dashed line, and solid line for the splash jet), $Fn = 1.2$ (dotted line, and solid line for the splash jet); (*b*) $\alpha = 45°$, $Fn = 10$ (solid line), $Fn = 2$ (dashed line); and (*c*) $\alpha = 60°$, $Fn = 10$ (solid line), $Fn = 3.2$ (dashed line). The open circles show the stagnation point. The two solid lines at the top left of panel (*c*) are the splash jet for $Fn = 10$ in the region of its maximal elevation.

the plate is unity. The interaction between the splash jet and the main incoming flow is not considered. Mathematically, this means that the splash jet moves to the second sheet of the Riemann surface (Ahlfors 1966). It can be seen from figure 3 that the length of the wetted surface of the plate and the vertical coordinate of the trailing edge of the plate increase with the Froude number. In figure 3(*a*), the trailing edge of the plate is above the undisturbed free surface for $Fn = 10$ and $Fn = 3$. It may seem from figure 3(*a*) that the free surface is all above the mean water level. However, the figure shows only the part of the computational domain near the plate, which is above the undisturbed free surface as discussed above. The whole shape of the free surface is similar to that shown in figure 2(*a*), i.e. the average level of the free surface upstream (from the plate to minus infinity) remains zero. A similar result can be observed at larger Froude number for $\alpha = 45°$ and $\alpha = 60°$ in figure 3(*b*,*c*), respectively.

For a practical boat at forward speed, its draught is determined by the balance between gravity and the fluid force in the vertical direction. It is often seen that this draught will reduce significantly and the body begin to glide on the surface when the speed increases further and further. On the other hand, figure 3 indicates that, when the path of the fluid is blocked by the plate, the water surface near the plate will rise up. At larger Froude number, or smaller gravity effect, the water surface will rise even higher. It may then be possible from the mathematical solution that, even when the moving plate is lifted above the mean water level, the plate is still in touch with

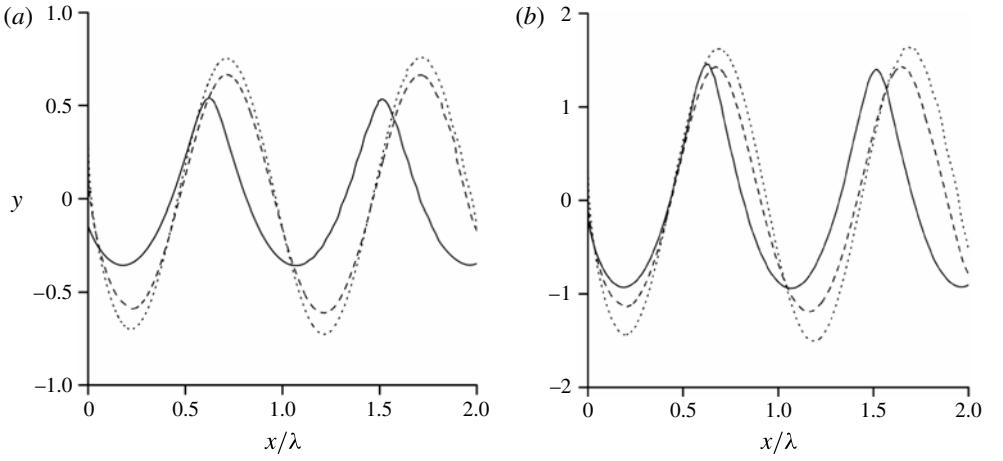


FIGURE 4. Free surface waves generated by the flat plate at the attack angle: (*a*) $\alpha = 20°$, $Fn = 1.2$ (solid line), $Fn = 3$ (dashed line), $Fn = 10$ (dotted line); and (*b*) $\alpha = 45°$, $Fn = 1.2$ (solid line), $Fn = 3$ (dashed line), $Fn = 10$ (dotted line).

the elevated water. Of course, such an observation can be conclusive only through experiments. However, this is a big challenge, as the Froude number corresponding to such a result is quite large, and could be even larger for a practical 3D body due to transverse flow.

It has been found for attack angle $\alpha > 50°$ that the splash jet may reach near to the maximal height $Fn^2/2$ at which the velocity on the top of the splash jet is zero. In such cases the splash jet is similar to the jet emerging from a nozzle and falling under gravity (Dias & Vanden-Broeck 1990). At the limit, the free surface may form a corner of angle 120° at the top of the splash jet. In figure 3(*c*) for $Fn = 3.2$ and $\alpha > 60°$, the maximal coordinate of the splash jet, $y_m$, approaches its maximal height $Fn^2/2 = 5.12$ shown by the dotted line and gives a ratio of $y/y_m = 0.98$, while for the case $Fn = 10$ shown by the solid lines the ratio is $y/y_m = 0.79$. Thus, when the Froude number decreases, the top of the splash jet approaches its maximal height and may tend to form a corner point. Such behaviour of the splash jet restricts the present computations for lower Froude numbers. In some cases cutting off the top of the splash jet makes it possible to extend the calculations for lower Froude numbers, but this may introduce uncertainty into the reliability of the result.

The free surface waves behind the flat plate corresponding to cases (*a*) and (*b*) in figure 3 are shown in figure 4, in which the horizontal scale has been normalized by the wavelength $\lambda = 2\pi Fn^2$, which comes from the linear theory of progressive waves. Any departure of the wavelength from this value is obviously due to the nonlinear effect. For Froude numbers $Fn = 10$ and $Fn = 3$, the shape of the free surface wave resembles more a sinusoidal curve than that at $Fn = 1.2$. In the latter case the wave crest becomes larger and sharper than the wave trough. Similar wave profiles were obtained by Vanden-Broeck (1980) for stern waves behind a semi-infinite body of constant draught. The pressure distribution on the plate is shown in figure 5 for $\alpha = 20°$ and $\alpha = 45°$ at different Froude numbers. For $\alpha = 20°$ and $Fn = 10$, the maximum pressure occurs near the stagnation point and its value is approximately equal to unity, which can be understood from (2.3). For smaller Froude numbers (larger gravity effect), the maximum pressure coefficient decreases. For the case

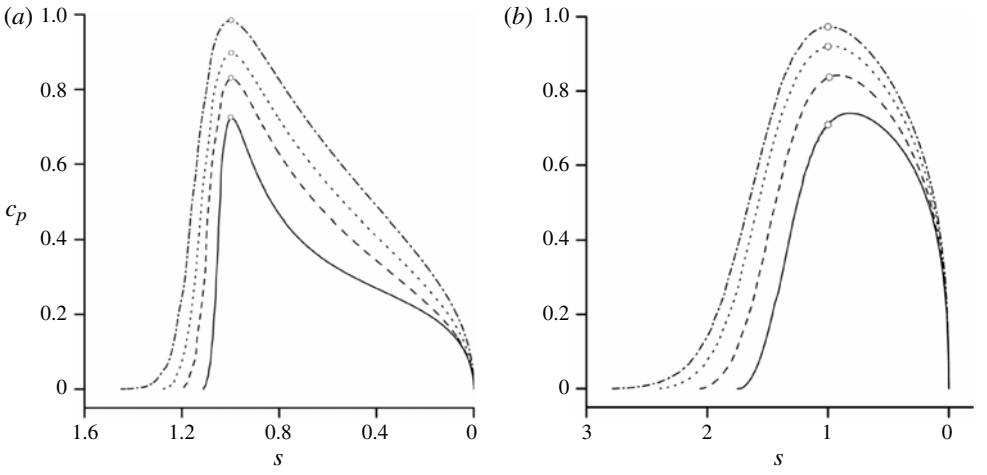


FIGURE 5. Pressure distribution along the flat plate: (*a*) $\alpha = 20°$, $Fn = 1.2$ (solid line), $Fn = 2$ (dashed line), $Fn = 3$ (dotted lines) and $Fn = 10$ (dash-dotted lines); and (*b*) $\alpha = 45°$, $Fn = 2$ (solid line), $Fn = 3$ (dashed line), $Fn = 5$ (dotted lines) and $Fn = 10$ (dash-dotted lines). The open circles show the stagnation point.

of $\alpha = 45°$, the location corresponding to the maximum pressure shifts slightly towards the trailing edge. The ends of the curves in figure 5 correspond to the points of flow separation from the plate. The decrease of the wetted length of the plate with the Froude number can be seen from the figure. We notice that, near a sharp trailing edge, the derivative of the pressure coefficient behaves like

$$\frac{\mathrm{d}c_p}{\mathrm{d}s} \sim \frac{1}{\sqrt{s}}, \quad s \to 0. \tag{3.6}$$

By differentiating (2.3) and recalling that $\mathrm{d}y/\mathrm{d}s = \sin\delta$, we find

$$\frac{\mathrm{d}c_p}{\mathrm{d}s} = \frac{\mathrm{d}c_p}{\mathrm{d}\xi} \Big/ \frac{\mathrm{d}s}{\mathrm{d}\xi} = -2v\frac{\mathrm{d}v}{\mathrm{d}\xi} \Big/ \frac{\mathrm{d}s}{\mathrm{d}\xi} - \frac{2\sin\delta}{Fn^2}. \tag{3.7}$$

Differentiating the function $v(\xi) = |\mathrm{d}w/\mathrm{d}z|_{\zeta=\xi}$ obtained from (2.8) for $\zeta = \xi$, we obtain

$$\frac{\mathrm{d}v}{\mathrm{d}\xi} = v(\xi)\left[\frac{2a}{\xi^2 - a^2} - \frac{1}{\pi}\int_0^\infty \frac{\mathrm{d}\beta}{\mathrm{d}\xi'}\frac{2\xi'}{\xi'^2 - \xi^2}\,\mathrm{d}\xi' + \frac{1}{\pi}\int_0^\infty \frac{\mathrm{d}\ln v}{\mathrm{d}\eta}\frac{2\eta}{\eta^2 + \xi^2}\,\mathrm{d}\eta\right] \tag{3.8}$$

and

$$\lim_{\xi\to 0}\frac{\mathrm{d}\ln v}{\mathrm{d}\xi} = -\frac{2}{a} - \frac{2}{\pi}\int_0^\infty \frac{\mathrm{d}\beta}{\mathrm{d}\xi}\frac{\mathrm{d}\xi}{\xi} + \frac{2}{\pi}\int_0^\infty \frac{\mathrm{d}\ln v}{\mathrm{d}\eta}\frac{\mathrm{d}\eta}{\eta}. \tag{3.9}$$

The above limit is equal to zero only for the case of smooth separation, as follows from (2.36). For other cases, $\lim_{\xi\to 0}(\mathrm{d}\ln v/\mathrm{d}\xi) \neq 0$. From (2.10) it is seen that the derivative of function $s(\xi)$ behaves as $\mathrm{d}s/\mathrm{d}\xi \sim \xi$ for $\xi \to 0$, i.e. $s(\xi) \sim \xi^2$, or $\xi \sim \sqrt{s}$. By substituting $\mathrm{d}s/\mathrm{d}\xi \sim \sqrt{s}$ in (3.7) and taking into account $\lim_{\xi\to 0}(\mathrm{d}\ln v/\mathrm{d}\xi) \neq 0$, we arrive at (3.6).

Some tabulated results for the wetted length $s_b$, the position of the trailing edge $h$, the force coefficient perpendicular to the plate $C_n$, the flow rate $q$ in the splash

| $\alpha = 10^\circ$ | | | | | | $\alpha = 20^\circ$ | | | | | |
|---|---|---|---|---|---|---|---|---|---|---|---|
| $Fn$ | $s_b$ | $h$ | $C_n$ | $q$ | $h_w$ | $Fn$ | $s_b$ | $h$ | $C_n$ | $q$ | $h_w$ |
| 20 | 1.15 | −0.385 | 0.431 | 0.0188 | 0.842 | 20 | 1.5 | −0.623 | 0.742 | 0.0653 | 1.483 |
| 10 | 1.14 | −0.28 | 0.424 | 0.0184 | 0.839 | 10 | 1.46 | −0.427 | 0.728 | 0.0636 | 1.482 |
| 5 | 1.12 | −0.173 | 0.4 | 0.0168 | 0.802 | 5 | 1.37 | −0.27 | 0.682 | 0.0584 | 1.409 |
| 3 | 1.09 | −0.083 | 0.354 | 0.0139 | 0.719 | 3 | 1.29 | −0.119 | 0.603 | 0.0489 | 1.281 |
| 2 | 1.07 | −0.007 | 0.294 | 0.0102 | 0.604 | 2 | 1.21 | 0.004 | 0.505 | 0.037 | 1.098 |
| 1.5 | 1.05 | 0.044 | 0.242 | 0.0074 | 0.5 | 1.5 | 1.15 | 0.088 | 0.427 | 0.0274 | 0.957 |
| 1 | 1.03 | 0.1 | 0.187 | 0.0041 | 0.376 | 1.2 | 1.11 | 0.144 | 0.375 | 0.0205 | 0.897 |
| 0.8 | 1.02 | 0.118 | 0.172 | 0.0028 | 0.368 | | | | | | |

TABLE 1. Results for $s_b$, $h$, $C_n$, $q$ and wave height $h_w$ for the flat plate at various Froude numbers and two attack angles.

jet and the wave height $h_w$ are presented in table 1 at different Froude numbers and attack angles. It is seen from table 1 that the flow rates $q$ are in the range 0.0028 at $Fn = 0.8$ and $\alpha = 10^\circ$ to 0.0653 at $Fn = 20$ and $\alpha = 20^\circ$. The disturbance to the main flow caused by the impact of the splash jet in real situations is proportional to the magnitude $q$. On the other hand, the magnitude of the velocity induced by gliding is of the order of unity. This justifies the assumption in the mathematical model that any disturbance caused by the impact of the splash jet is relatively small and can be ignored. The tabulated results are also shown in figure 6 using a logarithmic scale on the $x$-axis. As discussed above, for each angle of the plate there is some minimal Froude number corresponding to wave breaking in splash jet or downstream. The boundary of the region where a wave may break is shown by the dash-dot-dot line in figure 6($a$–$d$). From the figure it can be seen that all these parameters excluding the immersion of the trailing edge seem to tend to some finite values when $Fn \to \infty$ corresponding to zero gravity. The immersion of the trailing edge decreases linearly with the increase of the logarithm of the Froude number, as seen from 6($a$), i.e. $h \sim -\log Fn$. These results are consistent with Green's solution (Green 1936) for a weightless fluid, $Fn = \infty$, according to which the elevation of the body relative to the undisturbed free surface at infinity tends to infinity as $y \sim \log(1 + 1/|x|)$ for $x \to 0$ where the body location is assumed. Our explanation for this is based on the Bernoulli equation. If the incoming velocity is very large (or for large Froude number), the free surface near the body will increase because of the reduced velocity, in order to maintain the Bernoulli constant. Thus if the Froude number tends to infinity (which is the same as the gravity tending to zero), the level of the free surface near the body tends to infinity.

### 3.3. *Planing circular cylinder*

We consider another case in which the flow passes a surface-piercing circular cylinder. We use the radius of the cylinder, $R$, as the length scale, i.e. $L = R$, in the definition of the Froude number in (2.2) and in non-dimensionalization. The solutions are determined by two variables: the Froude number, $Fn$; and the length of the wetted part of the cylinder between points $O$ and $A$, $s_A$. The solution is obtained by assuming the initial value $\beta_0 = 0$ or $O$ at the bottom of the cylinder, and its final value is obtained when convergence has been achieved. The angles of flow separation at points $O$ and $B$ relative to the vertical line passing through the centre of the cylinder are $\alpha_1$ and $\alpha_2$, respectively, as shown in figure 7, together with $\theta$, which is the angle

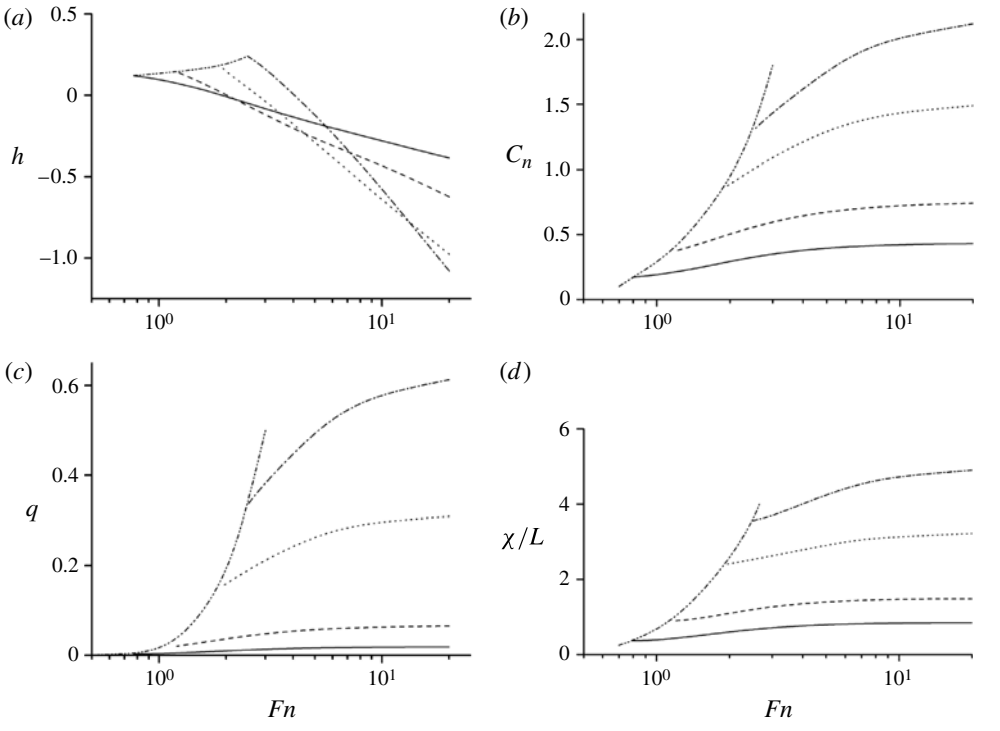


FIGURE 6. Results against the Froude number for (*a*) the submergence of the flat plat, (*b*) the normal force coefficient, (*c*) the flow rate of the splash jet and (*d*) the wave height downstream, for the angle of the plate 10° (solid line), 20° (dashed line), 45° (dotted line) and 60° (dash-dotted line).

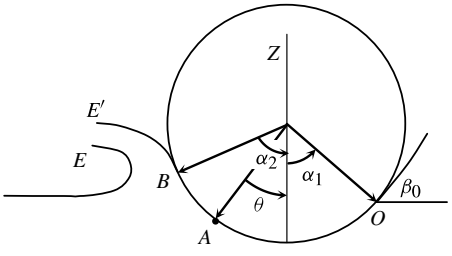


FIGURE 7. Definition sketch for the flow past a circular cylinder.

for the stagnation point $A$. The angle is positive when it is on the right-hand side of the vertical line. For the case of a circular cylinder, it is convenient to undertake computation for a fixed $\theta$, or the stagnation point $A$. In each iteration, when the location $O$ is obtained by imposing (2.36), $s_A$ can be obtained through $s_A = \alpha_1 - \theta$ in which $\alpha_1 = \beta_0$ for the case of a circular cylinder. When the results have converged, the wetted lengths $s^* = \alpha_1 - \alpha_2$ can be found from the solution.

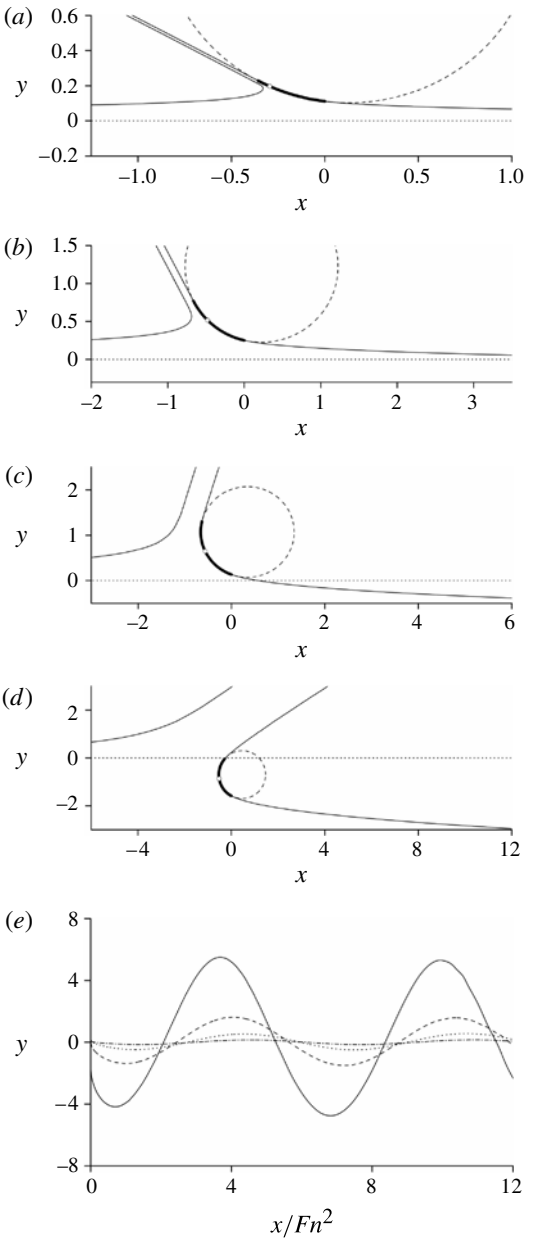


FIGURE 8. The free surface profile at Froude number $Fn = 10$ for (*a*) $\theta = -25°$, (*b*) $\theta = -45°$, (*c*) $\theta = -65°$ and (*d*) $\theta = -80°$. (*e*) The waves downstream for cases (*a–d*): dash-dotted, dotted, dashed and solid lines, respectively.

The free surface profiles for Froude number $Fn = 10$ at several angles $\theta$ are shown in figure 8. The wetted length in figure 8 is shown by the thick line on which the open circle indicates the location of the stagnation point corresponding to given angle $\theta$. For all these cases the splash jet forms almost a straight line near the cylinder due to the small effect of gravity. When the fixed stagnation point moves up on the front

| $\theta$ | $\alpha_1$ | $\alpha_2$ | $s_A = \alpha_1 - \theta$ | $s_B = \theta - \alpha_2$ | $s^* = s_A + s_B$ | $D$ |
|---|---|---|---|---|---|---|
| | | | | $Fn = 10$ | | |
| −25 | −7.3 | −29 | 0.308 | 0.07 | 0.378 | −0.103 |
| −45 | −13.1 | −62.2 | 0.557 | 0.3 | 0.857 | −0.225 |
| −65 | −20 | −105.9 | 0.785 | 0.715 | 1.5 | −0.073 |
| −80 | −27.7 | −132.2 | 0.912 | 0.911 | 1.823 | 1.745 |
| | | | | $Fn = 1$ | | |
| −10 | −3.82 | −10.3 | 0.108 | 0.005 | 0.113 | −0.002 |
| −25 | −10.4 | −27.3 | 0.255 | 0.04 | 0.295 | 0.0269 |
| −40 | −16.3 | −46.3 | 0.413 | 0.11 | 0.523 | 0.1143 |
| | | | | $Fn = 0.3$ | | |
| −5 | −3 | −5 | 0.036 | 0.00033 | 0.036 | 0.0014 |
| −10 | 2.57 | −12.7 | 0.219 | 0.00175 | 0.221 | 0.0086 |
| −16 | 15.2 | −16.7 | 0.544 | 0.01222 | 0.556 | 0.0268 |

TABLE 2. Locations of flow separation and stagnation point for cases shown in figures 8–10.

side from figure 8(*a–d*), the elevation of the cylinder increases from case (*a*) to case (*b*) and then decreases from case (*b*) to case (*d*), and the immersion $h$ become positive for case (*d*).

At large Froude number, or when the effect of gravity is negligible, the numerical results suggest that, when the angle $\theta \to -90°$ (see figure 7), $h \to -\infty$. The flow tends to be symmetric about the horizontal diameter of the cylinder. Such a case corresponds to a cylinder in an unbounded liquid with a cavity behind the body.

Some detailed results from figure 8 are given in table 2, together with the results from figures 9 and 10. It is seen from the table that the length $s_B$ between points $A$ and $B$ increases faster than $s_A$ with the increase of the magnitude of angle $\theta$. At $Fn = 10$ and $\theta = -80°$, we have $s_b \approx s_A$, which means that the wetted lengths on both sides of $A$ are about the same.

The free surface waves behind the cylinder at Froude number $Fn = 10$ are shown in figure 8(*e*) for cases (*a–d*). Although the wave amplitude increases with the magnitude of the angle $\theta$, all the curves resemble sinusoidal shape with the mean line near the undisturbed free surface.

The free surface profiles for Froude number $Fn = 1$ and at $\theta = -25°$ and $\theta = -40°$ are shown in figure 9(*a*,*b*), respectively. The splash jet detaches from the cylinder at a point closer to the stagnation point, rises to some height and then falls down into the second Riemann sheet. In figure 9(*b*) it is seen that the maximal elevation of the splash jet is close to its highest possible value $y_m = Fn^2/2 = 0.5$ at which the velocity at the top point is zero for the given Froude number $Fn = 1$. By comparing the results in table 2 at $\theta = -25°$ for $Fn = 1$ and $Fn = 10$ it is seen that the increase of gravity reduces the total wetted length and the front separation point $B$ approaches the stagnation point $A$.

The corresponding wave profiles downstream are shown in figure 9(*c*). Together with table 2, it can be seen at a given $\theta$ that the larger wetted length corresponds to larger depth of immersion. The wave shape for the case $\theta = -40°$ differs significantly from the sinusoidal form and it tends to the limit case in which the wave crest would tend to a corner point. This prevents the calculation for the case of the magnitude of $\theta$

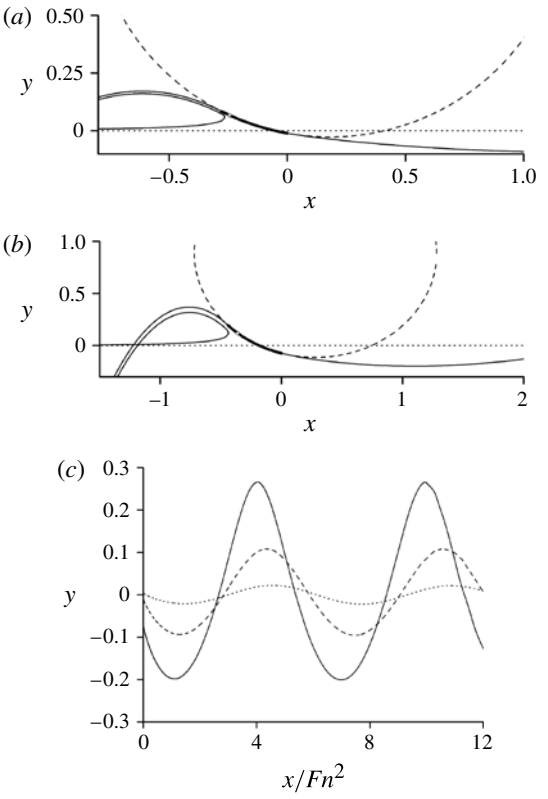


FIGURE 9. The free surface profile at Froude number $Fn = 1$ for (*a*) $\theta = -25°$ and (*b*) $\theta = -40°$. (*c*) The waves downstream for three cases: solid, dashed and dotted lines correspond to $\theta = -25°$, $\theta = -40°$ and $\theta = -10°$, respectively.

larger than 40°. For all the cases in figures 8 and 9 the rear separation at point $O$ is in fact on the front side of the cylinder, or $\alpha_1 < 0$.

The free surface profile for $Fn = 0.3$ and at $\theta = -5, -10$ and $-16°$ are shown in figure 10. Together with table 2, it can be seen that the depth of immersion increases with the magnitude of angle $\theta$. For this Froude number, the separation point $O$ is on the front part of the cylinder at $\theta = -5°$ and then moves to the back part at $\theta = -10°$ and $\theta = -16°$; correspondingly, $\alpha_1$ changes from negative to positive. When the magnitude of $\theta$ increases, the depth of immersion also increases as well as the distance between projections of points $O$ and $B$ on the $x$-axis. From figure 10(*c*) at $\theta = -16°$, it is seen that $y_O > 0$ and the distance $x_O - x_B$ is larger than the half-wavelength, i.e. $x_O - x_B > \lambda/2$, and the wetted part of the cylinder completely occupies the wave trough.

The splash jet for the cases in figure 10(*a*,*b*) is so thin that its computed length, which is ∼100 times its thickness, is still hardly visible. Besides, the separation point $B$ is close to the stagnation point but its velocity is not close to zero, since the vertical coordinate of the separation point is not close to the maximal height $y_m = Fn^2/2 = 0.045$. Comparing the coordinates of the stagnation points in figures 9 and 10, we can see that, with decrease of the Froude number, the stagnation point and separation point $B$ move towards each other and the undisturbed free surface. The

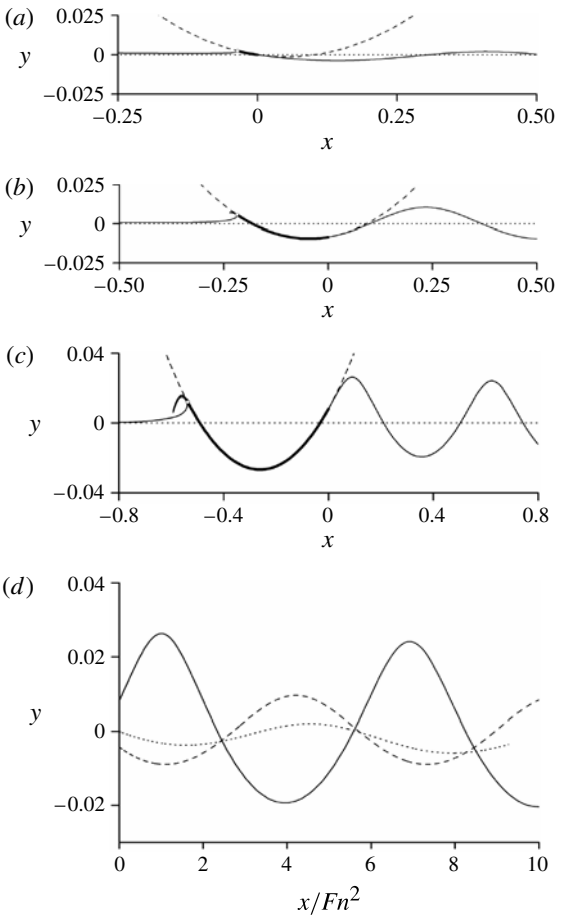


FIGURE 10. The free surface profile at Froude number $Fn = 0.3$ for (*a*) $\theta = -5°$, (*b*) $\theta = -10°$ and (*c*) $\theta = -16°$. (*d*) The waves downstream for the cases in (*a–c*): dotted, dashed and solid lines, respectively. The open circle is for the stagnation point.

approach of the stagnation point to the free surface was discussed by Yeung (1991) in a similar problem through numerical simulation.

The wave profiles downstream corresponding to cases (*a–c*) are shown in figure 10(*d*). We notice that the $y$ coordinate at $x = 0$ is $-h$. It can then be seen that the wave profiles change their phase relative to the cylinder.

Figure 11 gives the wave profile downstream of the planing cylinder calculated for Froude number $Fn = 0.5$ and the angle $\theta = -25°$. The ratio of the wave height, $h_w$, to the wavelength, $\lambda_n$, is found to be $h_w/\lambda_n = 0.10$. For the same ratio, results based on the Stokes second-order theory are taken manually from Schwartz (1974) and they are included in the figure together with the fully nonlinear numerical result (Greco, 2006, personal communication). The present result agrees very well with Greco's results lying underneath the solid line, and there is a small difference with the Stokes second-order theory.

The angles $\alpha_1$ and $\alpha_2$ at separation points $O$ and $B$, respectively, as functions of the angle $\theta$ for various Froude numbers are shown in figure 12. The solid

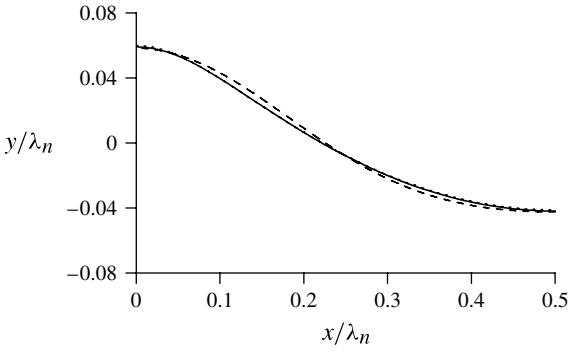


FIGURE 11. Downstream free surface wave, at Froude number $Fn = 0.5$ and angle $\theta = -25°$: solid line, present result; dashed line, second-order Stokes theory; dotted line, fully nonlinear numerical result.

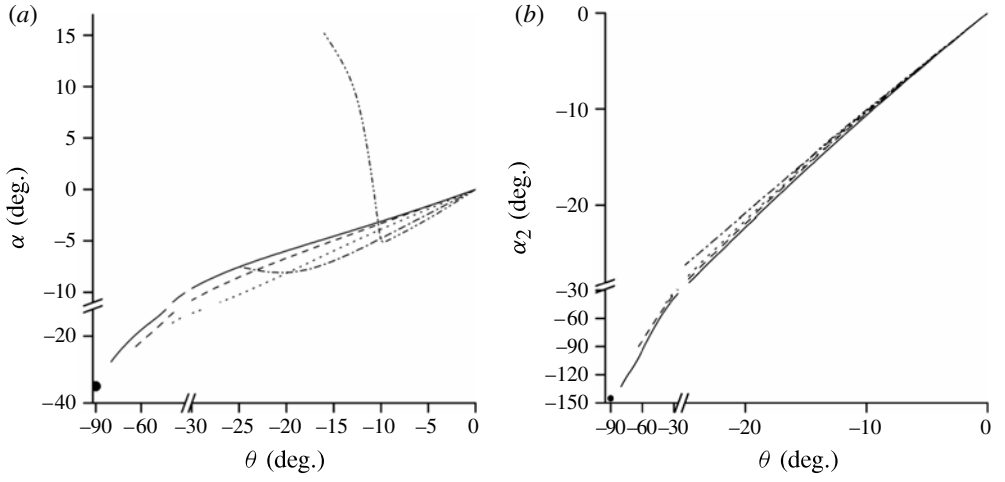


FIGURE 12. Angle at flow separation points (*a*) *O* and (*b*) *B*, for Froude number $Fn = 10$ (solid line), $Fn = 2$ (dashed line), $Fn = 1$ (dotted line), $Fn = 0.5$ (dash-dotted line) and $Fn = 0.3$ (dash-dot-dot line).

line corresponding to Froude number $Fn = 10$ changes approximately linearly with decrease of angle $\theta$ and tends to the value $\alpha_1 \approx -35°$ at $\theta = -90°$ shown by the solid circle, which is the angle of flow separation in an unbounded fluid domain of the weightless fluid Gurevich (1979). For Froude numbers $Fn = 2$ (dashed line) and $Fn = 1$ (dotted line), it is seen that larger gravity leads to a larger magnitude of angle $\alpha_1$ in the whole range of angle $\theta$. The opposite effect of gravity occurs for Froude number $Fn = 0.3$ (dash-dot-dot line) when the separation point *O* moves to the back part of the cylinder.

The angle of flow separation at *B* related to the splash jet, $\alpha_2$, changes approximately linearly with decrease of angle $\theta$ for all Froude numbers, as shown in figure 12(*b*). For Froude number $Fn = 10$ (the solid line), the angle $\alpha_2$ tends to the value $-145°$ at $\theta = -90°$ shown by the solid circle, which corresponds to the angle

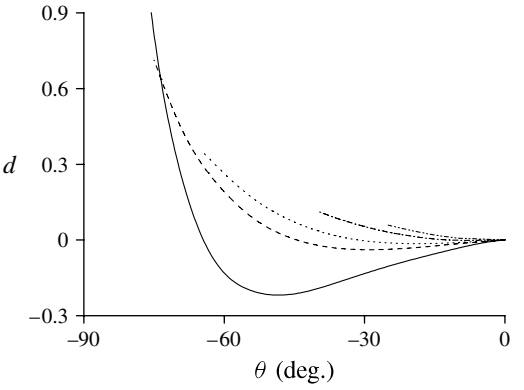


FIGURE 13. The depth of immersion, $d$, for Froude number $Fn = 10$ (solid line), $Fn = 3$ (dashed line), $Fn = 2$ (dotted line), $Fn = 1$ (dash-dotted line) and $Fn = 0.5$ (dash-dot-dot line).

of flow separation in the unbounded fluid domain of a weightless fluid and forms the mirror image of $\alpha_1 \approx -35^\circ$ in figure 12(*a*).

The depth of immersion, $d = D/R$, as a function of angle $\theta$ is shown in figure 13 for various Froude numbers. For each Froude number (it is visible in figure 13 only for $Fn > 1$) there is a range of angles $\theta_0 < \theta < 0$ for which the immersion is negative, i.e. the position of the cylinder is above the undisturbed free surface. Here, the angle $\theta_0$ corresponds to the zero depth of immersion for which the wetted length does not tend to zero. In the range $\theta_0 < \theta < 0$ two different $\theta$ with different wetted length may give the same $d$. The range of negative immersions and the maximal elevation of the cylinder above the undisturbed free surface increase with the increase of the Froude number. The ends of the curves in figure 13 for $Fn < 2$ are close to the maximal depth of immersion for which non-breaking waves downstream can be computed.

The pressure distribution on the wetted part of the cylinder is shown in figure 14 at different Froude numbers for cases at which the stagnation point is fixed on the cylinder at the angle $\theta = -35^\circ$. The negative $s - s_A$ correspond to the wetted part $OA$ and positive to $AB$. The ends of the curves in figure 14 correspond to the points of flow separation, $O$ and $B$, where the pressure coefficient is equal to zero. The maximum value of the pressure coefficient occurs near the stagnation point $A$ at which $s - s_A = 0$. It is seen that, for smaller Froude numbers, the maximum pressure coefficient decreases as well as the wetted length of the cylinder. From figure 14(*b*,*c*), it is clearly seen that the derivative tends to zero at both separation points according to conditions (2.36) or (2.37), which are equivalent. Such a pressure distribution near the separation point is different from that shown in figure 5 at $s = 0$ for the case of separation at the trailing edge of the flat plate, where the condition $\mathrm{d}c_p/\mathrm{d}s = 0$ is not used.

The drag $F_D$ and lift $F_L$ are evaluated by integrating the pressure along the wetted part of the cylinder. Using the radius of the cylinder as a reference length in the definition of the drag and lift coefficients,

$$C_D = \frac{F_D}{\rho U^2 R}, \quad C_L = \frac{F_L}{\rho U^2 R}, \tag{3.10}$$

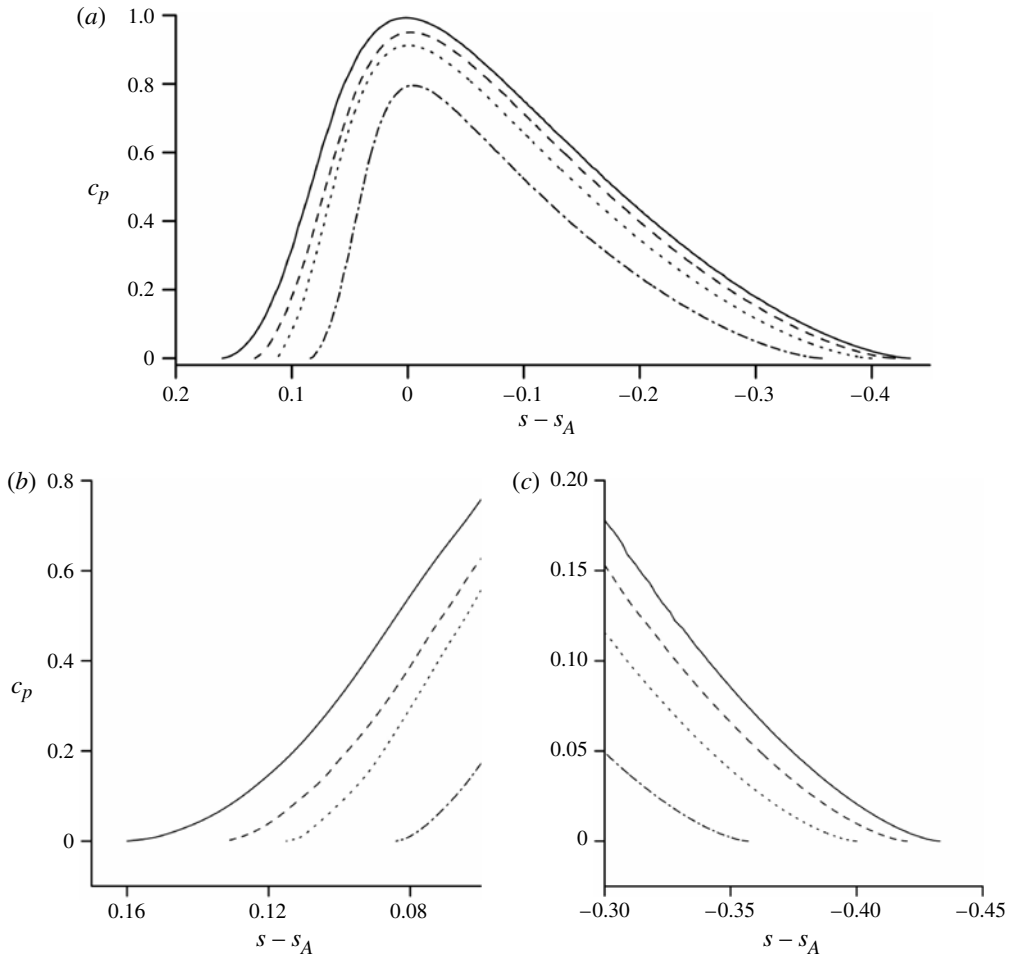


FIGURE 14. (*a*) Pressure distribution along the circular cylinder for $\theta = -35°$: $Fn = 10$ (solid line), $Fn = 3$ (dashed line), $Fn = 2$ (dotted lines) and $Fn = 1$ (dash-dotted lines). (*b*) and (*c*) The same near separation points $B$ and $O$, respectively.

we can obtain the expression

$$C_D + \mathrm{i}C_L = -\frac{\mathrm{i}}{2}\int_0^b \left(1 - v^2(\xi) - \frac{2y(\xi)}{Fn^2}\right)\left.\frac{\mathrm{d}z}{\mathrm{d}\zeta}\right|_{\zeta=\xi} \mathrm{d}\xi, \tag{3.11}$$

where the velocity magnitude $v(\xi) = |\mathrm{d}w/\mathrm{d}z|_{\zeta=\xi}$ and the coordinate $y(\xi) = \mathrm{Im}[z(\zeta)|_{\zeta=\xi}]$ are obtained from (2.8) and (2.10), respectively.

The results of the lift and drag coefficients are shown in figure 15. For Froude number $Fn = 10$, the lift coefficient reaches its maximum value at $\theta \approx -55°$, then decreases and tends to zero as $\theta \to -90°$, since this case corresponds to the symmetric free streamline flow in the unbounded fluid domain. The drag coefficient monotonically increases with the magnitude of $\theta$ and for $\theta \to -90°$ tends to its maximal value $C_D = 0.4895$ taken from Gurevich (1979) and shown by the solid circle in figure 15(*b*). From figure 15 it is seen that the decrease of Froude number leads to the decrease of the lift and drag coefficients except for the case of Froude

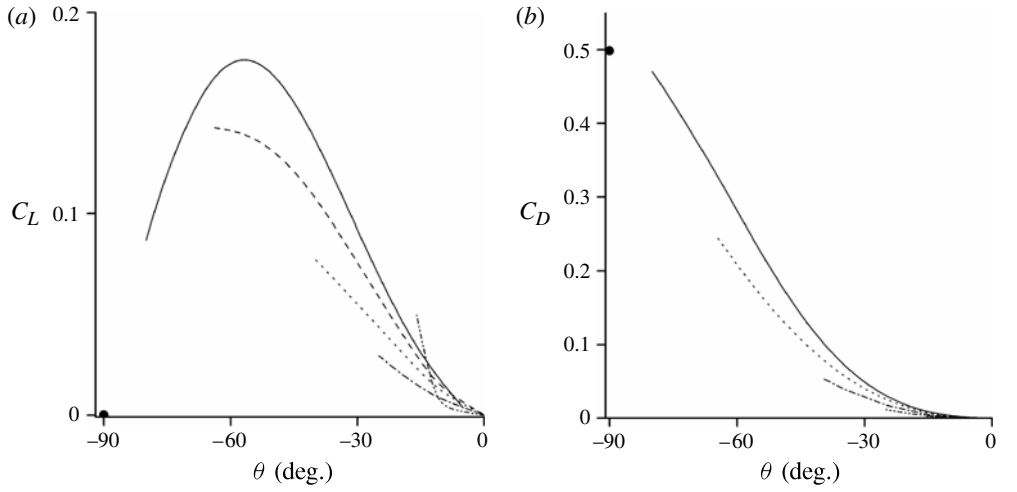


FIGURE 15. (*a*) Lift and (*b*) drag coefficients for Froude number $Fn = 10$ (solid line), $Fn = 2$ (dashed line), $Fn = 1$ (dotted line), $Fn = 0.5$ (dash-dotted line) and $Fn = 0.3$ (dash-dot-dot line).

number $Fn = 0.3$ for which it has been noticed that the flow separation point $O$ moves from the front to the back part of the cylinder. We note again that the left ends of the curves in figure 15 correspond to the limit cases for which non-breaking waves downstream of the cylinder can be computed.

## 4. Conclusions

The problem with the fully nonlinear boundary condition for the flow generated by a body gliding along the free surface in the presence of gravity has been solved. The integral hodograph method has been employed to derive the analytical expressions for the governing functions, which are the complex velocity and the derivative of the complex potential in a parameter plane. The combination of these functions gives the function conformally mapping the parameter plane onto the physical plane. These governing functions explicitly contain the unknown constants, singular points and the velocity magnitude on the free surface as well as the slope of the body on its wetted part as functions of the parameter variable. The problem is then converted into a system of integral and integro-differential equations in terms of these unknown functions after the dynamic and kinematic boundary conditions on the free surface are imposed. The adopted Brillouin–Villat criterion in terms of the zero pressure gradient at the intersection point has made it possible to determine the locations of separation of the main flow and the splash jet from the body.

The numerical results for a flat plate and for a circular cylinder are presented over a wide range of Froude numbers, in terms of the free surface shape, the wetted length of the body, the wave profile downstream, the depth of immersion, the locations of flow separation, the flow rate at the splash jet, and the drag and lift coefficients.

For the case of a flat plate, solutions are obtained in terms of the given angle of the plate and the Froude number based on the length between the trailing edge and the stagnation point. The depth of immersion, the total wetted length of the plate and all other flow parameters are functions of these parameters. The results obtained

have revealed that both positive and negative depths of immersion, corresponding to the plate being below or above the undisturbed free surface, may be possible. From the calculations it follows that the elevation of the plate above the undisturbed free surface behaves like $h \sim -\log Fn$ when $Fn \to \infty$. This result agrees with the so-called Green's paradox for an ideal weightless fluid. At the same time, the amplitude of the downstream waves, $h_w$, tends to some finite value, and therefore the ratio $h_w/h \to 0$ as $Fn \to \infty$. The nonlinearity of the problem is reflected in some reduction of the wavelength. The pressure distribution along the plate shows a reduction as the Froude number decreases, reflecting the effect of gravity. It is also noticed that the maximum pressure could occur away from the stagnation point. The thickness and the flow rate of the splash jet decrease with decrease of the angle of the plate or the Froude number.

For the gliding cylinder, the results have revealed that, at a given position of the stagnation point, there may be two solutions for negative depths of immersion and only one for positive immersion. The former corresponds to two wetted lengths. For Froude numbers $Fn > 0.3$, it is noticed that the main flow separates on the front part of the cylinder, while for Froude numbers $Fn < 0.3$ separation could be either at the front or back of the body. In the latter case, the projection of the wetted length of the cylinder on the horizontal axis may become larger than a half-wavelength, i.e. the cylinder may occupy the wave trough completely. It is found that the solution of the problem tends to that corresponding to a weightless fluid and the depth of immersion tends to infinity, when the stagnation point tends to the farthest front point of the cylinder.

## Acknowledgements

This work is supported by Lloyd's Register Foundation (LRF) through the joint centre involving University College London, Shanghai Jiaotong University and Harbin Engineering University, to which the authors are most grateful. LRF supports the advancement of engineering-related education, and funds research and development that enhances safety of life at sea, on land and in the air.

## REFERENCES

AHLFORS, L. V. 1966 *Complex Analysis*. McGraw-Hill.

BRILLOUIN, M. 1911 Les surfaces de glissement de Helmholtz et la resistance des fluids. *Ann. Chim. Phys.* **23**, 145–230.

CHAPLYGIN, S. A. 1910 About pressure of a flat flow on obstacles. In *On the Airplane Theory*. Moscow University, 49 pp.

CHEN, X. N. & WEI, R. J. 1994 Dynamic behaviour of a non-propagating soliton under a periodically modulated oscillation. *J. Fluid Mech.* **259**, 291–303.

DAGAN, G. & TULIN, M. P. 1972 Two-dimensional free surface gravity flow past blunt bodies. *J. Fluid Mech.* **51**, 529–543.

DIAS, F. & VANDEN-BROECK, J.-M. 1990 Flows emerging from a nozzle and falling under gravity. *J. Fluid Mech.* **213**, 465–477.

DIAS, F. & VANDEN-BROECK, J.-M. 1993 Nonlinear bow flows with spray. *J. Fluid Mech.* **255**, 91–102.

FALTINSEN, O. M. & SEMENOV, Y. A. 2008 The effect of gravity and cavitation on a hydrofoil near the free surface. *J. Fluid Mech.* **597**, 371–394.

GREEN, A. E. 1936 Note on the gliding of a plate on the surface of a stream. *Math. Proc. Cambr. Phil. Soc.* **32**, 248–252.

GUREVICH, M. I. 1965 *Theory of Jets in Ideal Fluids*. Academic.

GUREVICH, M. I. 1979 *Theory of Jets in Ideal Fluids*, 2nd edn. Nauka (in Russian).

GUREVICH, M. I. & YAMPOLSKY, A. R. 1933 On a moving of a planing flat-plate foil. *Tekhnika Vozdushnogo Flota* **10**, 52–70 (in Russian).

JOUKOVSKII, N. E. 1890 Modification of Kirchhoff's method for determination of a fluid motion in two directions at a fixed velocity given on the unknown streamline. *Math. Coll.* **15**, 121–278.

KOCHIN, N. E. 1938 Two-dimensional problem of the incompressible flow past a slightly arched planing hydrofoil under gravity. *Trudy TSAGI, Moscow*, vol. 356 (in Russian).

LATORRE, R. & RYAN, S. 1990 Study of the splash angle from a plate at small incidence angles and edge emergence. *Ocean Engng* **17** (3), 315–320.

SEDOV, L. I. 1937 Two-dimensional planing problem under gravity. *TSAGI, Moscow*, pp. 7–30 (in Russian).

SEMENOV, Y. A. 2003 Complex potential of an unsteady flow with a free boundary. *Vestnik Hersonskogo Univ., Herson, Ukraine* **2**, 384–387 (in Russian).

SEMENOV, Y. A. & CUMMINGS, L. J. 2006 Free boundary Darcy flows with surface tension: analytical and numerical study. *Eur. J. Appl. Math.* **17**, 607–631.

SEMENOV, YU. A. & IAFRATI, A. 2006 On the nonlinear water entry problem of asymmetric wedges. *J. Fluid Mech.* **547**, 231–256.

SCHWARTZ, L. W. 1974 Computer extension and analytic continuation of Stokes expansion for gravity waves. *J. Fluid Mech.* **62**, 553–578.

TUCK, E. O. 1982*a* Linearized planing-surface theory with surface tension. Part I. Smooth detachment. *J. Austral. Math. Soc. Ser.* B **22**, 241–258.

TUCK, E. O. 1982*b* Linearized planing-surface theory with surface tension. Part II. Detachment with discontinuous slope. *J. Austral. Math. Soc. Ser.* B **23**, 259–277.

VANDEN-BROECK, J.-M. 1980 Nonlinear stern waves. *J. Fluid Mech.* **96** (3), 603–611.

VANDEN-BROECK, J.-M. 1989 Bow flows in water of finite depth. *Phys. Fluids* A **1**, 1328–1330.

VANDEN-BROECK, J.-M. 2010 *Gravity–Capillary Free-Surface Flows*. Cambridge University Press.

VANDEN-BROECK, J.-M. & TUCK, E. O. 1977 Computation of near-bow or stern flows using series expansion in the Froude number. *Proceedings of the 2nd International Conference on Numerical Ship Hydrodynamics*, University of California.

VANDEN-BROECK, J. M., SCHWARTZ, L. W. & TUCK, E. O. 1978 Divergent low-Froude number series expansions of nonlinear free-surface flow problems. *Proc. R. Soc. Lond.* A **361**, 207–224.

VILLAT, H. 1914 Sur la validité des solutions de certains problèmes d'hydrodynamique. *J. Math Pure Appl.* **20**, 231–290.

WAGNER, H. 1932 On phenomena of impact and planing on a fluid surface. *Z. Angew. Math. Mech.* **12**, 193–215.

WANG, C. Z. & WU, G. X. 2006 An unstructured-mesh-based finite element simulation of wave interactions with non-wall-sided bodies. *J. Fluids Struct.* **22**, 441–461.

YEUNG, R. W. 1991 Nonlinear bow and stern waves – inviscid and viscous solutions. In *Mathematical Approaches in Hydrodynamics* (ed. T. Miloh), pp. 349–369. SIAM.

YOON, B. S. & SEMENOV, Y. A. 2011 Separated inviscid sheet flows. *J. Fluid Mech.* **678**, 511–534.